UILU-ENG 86-3609

Report No. 132

AN INVESTIGATION INTO ISOTHERMAL AND THERMO-MECHANICAL FATIGUE DAMAGE AT ELEVATED TEMPERATURES

by

Mark L. Karasek

Materials and Design Division
Department of Mechanical and Industrial Engineering

A Report of the

MATERIALS ENGINEERING - MECHANICAL BEHAVIOR

College of Engineering, University of Illinois at Urbana-Champaign

August 1986

ACKNOWLEDGMENT

This work was funded by the Association of American Railroads, Technical Center, Chicago, Illinois. The cooperation of Dr. Daniel Stone and Mr. Michael Fec of the AAR Technical Center is gratefully acknowledged.

I would also like to acknowledge the support and guidance of my advisor, Professor Huseyin Sehitoglu. His time spent in discussion and review of this work was greatly appreciated.

Mr. Don Slavik, graduate student, and Mr. Richard Neu, student worker, assisted in some of the thermo-mechanical fatigue experiments.

Finally, I would like to thank my parents for their continued support and encouragement throughout my education. They have provided me with the opportunities and the freedom to choose my own directions.

TABLE OF CONTENTS

LIST OF TABLES

LIST OF FIGURES

NOMENCLATURE

A_1, A_2	Area of bar 1, bar 2
a	Crack length
a_A, a_C	Activity of material A, material C
B_f	Blocks to failure
b	Fatigue strength exponent
c	Fatigue ductility exponent
D	Lattice diffusion coefficient
D_o	Diffusivity constant
d	Diameter
E	Modulus of elasticity
f	Fugacity
h_i	Oxide intrusion depth
h_o	Oxide thickness
K	Temperature dependent constant in pressure equation
k	Universal gas constant
ℓ_1, ℓ_2	Length of bar 1, bar 2
N/N_f	Fatigue life fraction
N_f	Cycles to failure
P	Gas partial pressure
Q	Activation energy
R	Stress ratio
T	Temperature
T_{max}	Maximum temperature of the thermal cycle
T_{mean}	Mean temperature of the thermal cycle
T_{min}	Minimum temperature of the thermal cycle
t	Time
t_f	Time to failure
t_{ox}	Time of oxidation
ΔG_o	Gibb's free energy
ΔT_{minor}	Minor temperature cycle range
$\Delta\varepsilon$	Strain range
$\Delta\varepsilon_m$	Mechanical strain range
$\Delta\varepsilon_p$	Plastic strain range

$\Delta\sigma$	Stress range
$\Delta\sigma/2$	Stress amplitude
$\dot{\varepsilon}$	Strain rate
$\dot{\varepsilon}_{av}$	Average strain rate
ε_f'	Fatigue ductility coefficient
σ_{max}	Maximum stress
σ_f'	Fatigue strength coefficient
Γ	Activity coefficient

1. INTRODUCTION

Thermo-mechanical fatigue problems are encountered in many engineering applications. Temperature and load cycling may occur in turbine blades, piping, pressure vessels, railroad wheels due to brake shoe action and other components which experience high temperatures in service. Fatigue damage (crack initiation and growth) under thermo-mechanical loading has not been examined as extensively as fatigue damage under isothermal loading. As a result, while isothermal tests at high temperatures have been performed and results are available for many materials, conditions exist where isothermal data fails to adequately predict thermo-mechanical damage. Further work is needed to establish the differences in material behavior for the two cases and provide a better understanding of the problem.

Since the interaction of many mechanical and environmental factors influence different materials in different ways, previous workers have used a variety of parameters to compare isothermal and thermo-mechanical fatigue. Some of the parameters used in previous studies to predict thermo-mechanical fatigue lives based on isothermal data include mechanical strain range ($\Delta\varepsilon_m$) [1-4], plastic strain range ($\Delta\varepsilon_p$) [1,5-8], stress amplitude ($\Delta\sigma/2$) [4,7], maximum stress (σ_{max}) [9], combination of maximum stress and mechanical strain range ($\sigma_{max}*\Delta\varepsilon_m/2$) [10], and the strain range partitioning approach [11]. While isothermal tests were usually performed at the maximum or mean thermo-mechanical test temperature, several researchers have also suggested equivalent temperature levels at which isothermal and thermo-mechanical fatigue would be similar [7,12]. In an earlier paper on the 1070 steel examined here, it

was shown that the use of the mechanical strain range parameter and isothermal data at the mean temperature of the thermo-mechanical tests resulted in nonconservative predictions [13]. The predictions improved when isothermal data corresponding to the maximum thermo-mechanical temperature was utilized [13]. Recently, bithermal experiments have been performed by NASA workers where tensile and compressive portions of the hysteresis loop occurred at high and low temperatures respectively (or vice versa) [14]. These tests combine high temperature and low temperature mechanisms with tension or compression and provide further insight into thermo-mechanical behavior. Multi-temperature tests where the temperature was stepped up and down in the range 20°C to 700°C during isothermal strain cycling have been reported [15,16]. These experiments examined the effects of temperature history on subsequent stress-strain response.

The influence of environment appears to be a key factor in interpreting experimental results and component behavior at high temperatures for many materials. Various environments may be present under service conditions and many have been studied in relation to thermal fatigue [17,18,19]. This study is concerned with material behavior of 0.7 percent C steel (Class U wheel steel) at high temperatures in air environment. As a result, the effects of air environments on steel at high temperatures will be emphasized below. However, the mechanisms and trends discussed here are applicable to cases involving other materials and environments, where additional mechanisms may also be present.

Surface oxidation of steels during thermal loading can accelerate crack initiation [10]. While there are numerous papers on oxidation

kinetics in steel [10,20-39], only a few have dealt with oxides formed during fatigue [34-39]. Iron oxides form by cation diffusion from the metal/oxide interface to the oxide/air interface, with a corresponding vacancy diffusion from the oxide/air interface to the metal/oxide interface. These vacancies migrate to vacancy sinks such as dislocations or lattice steps, which are abundant in cold worked materials. If insufficient vacancy sinks are available, as in an annealed material, pores are nucleated between the oxide and the metal leading to oxide decohesion.

The Pilling-Bedworth Ratio (PBR) of a metal-oxide system can be used to approximate the sign and magnitude of the oxide growth stresses due to differences in lattice dimensions between oxide and metal [21]. The PBR is defined as the ratio of the volume of the oxide to the volume of the metal for a constant number of metal ions. If the PBR is greater than 1, compressive stresses would be expected in the oxide layer. Reported values of PBR for iron-iron oxide range between 1.7 and 2.1 [21,22], indicating that compressive oxide stresses would develop during growth. Specimen geometry (local convexity of the surface, specimen diameter) can also affect oxide integrity [28]. For a cylindrical steel specimen, when the metal cations diffuse to the oxide/air interface, the diameter of the cylinder is reduced causing compressive hoop stresses in the oxide. This compressive hoop stress can result in delamination and subsequent buckling of thin oxide layers. If this layer detaches from the surface, the oxide layer is considered to have undergone spalling. The stress state would be different if the oxide growth occurred at the metal/oxide interface. Another factor which can contribute to oxide

stresses and decohesion is thermal expansion coefficient mismatch between oxide and metal, a problem accentuated in thermal cycling. It has been reported recently that between 470°C and 610°C the thermal expansion coefficient of Fe_3O_4 is almost twice as large as that of steel, while below 470°C the coefficients of expansion match closely [34]. It is likely that other oxide/metal systems exhibit similar effects. Cracking of an oxide layer could affect the subsequent oxidation rate by increasing the partial pressure of oxygen at the interface and thus affect crack initiation and growth into the metal. Compressive oxide stresses may lead to buckling of the oxide layer away from the metal substrate [35,36]. Exposed metal surfaces under buckled sections of the oxide layer may be subject to additional environmental attack forming new oxide layers, affecting crack initiation and promoting internal oxidation.

In addition, recent work has shown that the diffusion of gaseous species into a metal can lead to internal oxidation of impurities or precipitates [40,41]. As a result, high internal cavity pressures develop and act along with applied stresses to accelerate cavity growth due to creep [40,41]. Cavity formation and growth at precipitate particles is the dominant creep mechanism observed in this study.

Railroad wheels experience thermal loading during brake shoe applications. Thermal cracking of wheels under these conditions is a serious concern and has been studied extensively [42-46]. During brake applications, brake shoes would contact localized variations on the tread surface. These areas would be preferentially heated as compared to the surrounding material. Therefore, in addition to global temper-

ature cycling, hot spots develop on the tread of the wheel as it passes under the brake shoe. Thermal streses on the hot spots are higher than the relatively cooler surrounding material. The hot spots and other critical regions experience many small thermal cycles within major thermal cycles due to repeated brake applications. This process is simulated in this study by performing thermo-mechanical block tests, where minor temperature cycles occur at the high temperature end of the major cycle. In addition, environmental effects such as surface and internal oxidation can be important. While oxide formed on the tread is removed by the action of the brake shoe, oxide formation in the flange regions may be extensive and influence crack nucleation. In Fig. 1, oxide penetration into the wheel in the form of long thin intrusions is observed in a section of material taken from the tread of a railroad wheel which failed in service. High temperatures experienced in railroad wheel service could lead to increased oxygen diffusion and accelerated damage. Time-dependent deformation at high temperatures also influences residual stresses which develop upon cooling. The temperatures chosen for this study are in the range 150°C to 700°C and reflect those experienced by critical regions in railroad wheel service.

While there are substantial benefits of simulating temperature-strain histories on specimens and examining thermo-mechanical fatigue lives, it is chosen in this study to consider the simplest of temperature-strain histories. This provides a first step in understanding material behavior, crack growth, and environmental effects in thermal loading. In the future, more complicated histories could be devised and the interaction of a variety of mechanisms may be studied.

This study will compare fatigue lives, surface oxidation characteristics, and oxygen diffusion controlled cavity formation and growth under (a) isothermal constant amplitude, (b) thermo-mechanical constant amplitude, and (c) thermo-mechanical block loading conditions. The relationship between surface oxidation characteristics and internal cavity formation and growth will also be explored. In addition, discriminating tests under conditions of zero applied load (a) at constant temperature and (b) under thermal cycling will be performed to investigate the effect of oxide growth stresses on oxide structure. Interrupted isothermal and thermo-mechanical tests where specimens are sectioned after a certain fraction of the lifetime will provide insight into the accumulation of damage in oxide and metal.

2. EXPERIMENTAL PROCEDURE

2.1 Material

The material examined was a 1070 steel typically used in railroad wheels (class U wheel steel). The chemical composition of the steel is given in Table 1. The specimens were cut from the rim of a railroad wheel (50 mm below the tread) in the circumferential direction. The machined specimens had a uniform gage length of 25.4 mm and a diameter of 7.62 mm. The specimen geometry is shown in Fig. 2. A typical pearlitic microstructure shown in Fig. 3 was obtained. Pearlite colony size was 50 μm, with an average pearlite spacing of 0.5 μm.

2.2 Equipment

Tests were performed on a 20 kip MTS testing machine controlled with a PDP-11/05 computer. In thermo-mechanical tests, induction heating (Lepel 2.5 kW capacity) was used to heat the specimens. Thermocouples attached to the specimen provided input to the temperature controller which received the command signal from the PDP-11/05 computer. The temperature gradient over the gage section was minimized by optimization of the coil configuration. No forced cooling, which would generate thermal gradients, was used. The strain was measured over the gage length with a 25.4 mm axial extensometer utilizing quartz rods. The schematic of the test system is shown in Fig. 4. In isothermal tests certain specimens were tested using a resistance furnace (clamshell type) while induction heating with temperature control was used on other specimens. All specimens used for oxide comparison were tested using induction heating. The same specimen design was used for iso-

thermal and thermo-mechanical tests, allowing direct comparison of oxidation characteristics and crack growth behavior. Stress-strain data was recorded on floppy disk for later analysis.

After removal from the test frame, the specimens were sectioned using a low speed saw and were mounted in epoxy. The composition of oxides in the corrosion layers were identified by etching with a 1 percent solution of HCl in ethanol. A 5 percent Nital etch was used to evaluate the microstructure of the 1070 steel before and after testing. Scanning electron microscopy was used to obtain pictures of the specimen surface and oxidation characteristics. Auger spectroscopy was utilized for internal oxidation study.

2.3 Test Conditions

Experiments were conducted under isothermal and thermo-mechanical loading conditions. The isothermal fatigue life tests were performed under strain control in the temperature range 20°C to 700°C at strain amplitudes ranging from 0.0015 to 0.01. The strain rates considered were 0.02, 0.002, and 0.0002 sec^{-1}.

The thermo-mechanical tests were performed under total constraint and were out-of-phase (maximum strain at minimum temperature). A total constraint experiment involved clamping the specimen at the low temperature end and cycling the temperature while the net strain is maintained at zero. All the thermal strain is converted to mechanical strain in this case. An illustration of total constraint is given in Fig. 5 (parallel bar model) where Bar 1 is heated and cooled, while Bar 2 remains isothermal and has large stiffness (A_2/A_1 large) as compared to

Bar 1. Other loading conditions are possible with this model (A_2/A_1 not large) and have been considered in Ref. 47.

Two sets of thermo-mechanical fatigue life tests were performed: (a) constant amplitude tests with minimum temperatures of 150°C, 400°C, or 500°C and maximum temperatures ranging from 450°C to 700°C, (b) block tests where one block consisted of one major temperature cycle (T_{min} = 150°C, T_{max} = 500°C, 600°C, 650°C, or 700°C) followed by one hundred minor temperature cycles (temperature range = 100°C, 150°C, or 200°C) at the high temperature end. Combinations of maximum and minimum temperatures were chosen to simulate thermal cycling conditions experienced in railroad wheel service. Strain rates for heating were higher than strain rates for cooling, but the average strain rate for these tests was on the order of 0.0002 sec^{-1}. Heating and cooling times for thermo-mechanical tests ranged from 30 to 50 seconds and 120 to 180 seconds respectively. A typical example of experimental temperature-time variation is given in Fig. 6.

Two sets of interrupted tests were performed to examine the progression of surface oxidation and internal cavitation under thermal loading: (a) isothermal constant amplitude tests to 10 percent and 40 percent of fatigue life at 600°C with a strain amplitude of 0.0035 (N_f = 700 cycles, t_f = 15 hours), (b) thermo-mechanical constant amplitude tests to 10, 20, 30, 40, and 60 percents of fatigue life with a minimum temperature of 150°C and a maximum temperature of 600°C (N_f = 735 cycles, t_f = 30 hours). Temperatures chosen for the thermo-mechanical tests were indicative of those seen in railroad wheel service. Lower maximum temperatures would have made test time pro-

hibitive, while higher maximum temperatures would be unrealistic as compared to railroad wheel service temperatures. The mechanical strain range in the isothermal tests was approximately equal to that of the thermo-mechanical tests, and strain rates in all interrupted tests were on the order of 0.0002 sec^{-1} for both cases.

In addition, two tests were performed to investigate the effect of oxide growth stresses on oxide structure and cavity formation. The first test involved holding a specimen at 600°C while maintaining zero load. The duration of this test was 16 hours and was approximately equal to the test time for the 600°C isothermal test with a strain amplitude of 0.0035. The second test performed under zero load conditions involved subjecting a specimen to temperature cycling between 150°C and 600°C under free expansion conditions ($\varepsilon_m = 0$). The duration of this test was approximately equal to the test time for a total constraint test with identical temperature cycling (t = 30 hours).

3. EXPERIMENTAL RESULTS

3.1 Fatigue Life Tests

3.1.1 Fatigue Test Results And Predictions

Isothermal test results are shown in Tables 2 through 4. Strain-life curves were established from isothermal constant amplitude data for strain rates of 0.02 sec^{-1} and 0.0002 sec^{-1}, respectively. Above 400°C, a decrease in strain rate resulted in shorter fatigue lives for all strain amplitudes considered. The strain-life curves were represented by the total strain-life equation [48]. The resulting coefficients and exponents were established as a function of temperature and are listed in Tables 5 and 6. In general, fatigue lives decreased with increasing temperature. However, at 700°C ($\dot{\varepsilon}$ = 0.0002 sec^{-1}) lives are longer than at 600°C at corresponding strain levels.

Thermo-mechanical constant amplitude test results are presented in Table 7. The correlation between experimental constant amplitude thermo-mechanical lives and predicted lives calculated from isothermal data, as shown in Fig. 7, was discussed in a previous article (Ref. 49) and will only be mentioned briefly in this paper. The predicted lives were calculated based on isothermal tests at the same mechanical strain range and comparable strain rates, and at the maximum thermo-mechanical temperature. Experimental and predicted lives for the case T_{min} = 150°C show good agreement over a wide range of mechanical strain. When the mechanical strain range is small, the predicted lives are slightly non-conservative (experimental lives shorter than predicted lives). When the minimum temperature is 400°C or above, the predicted lives are highly nonconservative, as indicated in Fig. 7.

The experimental results of the thermo-mechanical block tests are shown in Table 8. Predicted blocks-to-failure for thermo-mechanical block loading were calculated using Miner's linear damage rule. Isothermal constant amplitude data was highly nonconservative in predicting thermo-mechanical block test lives, while predictions based on constant amplitude thermo-mechanical data were within a factor of 1.5 of experimental lives [49].

3.1.2 Material Response

Material response was discussed in a previous article [49] and will be considered briefly here. Typical stress-strain response for isothermal and thermo-mechanical loading are shown in Fig. 8. Maximum stresses and stress ranges for isothermal and thermo-mechanical loading are different even when mechanical strain ranges are similar. Material response in 1070 steel changes significantly with temperature [13] and strain rate [50] above 400°C. In thermo-mechanical loading, tensile mean stresses develop in all cases considered (Tables 7 and 8), while under fully reversed (R = -1) isothermal loading mean stress is zero (Tables 2-4). The maximum stresses in the major temperature cycles of the thermo-mechanical block tests are approximately equal to the maximum stresses in the thermo-mechanical constant amplitude tests. However, the maximum stresses in the minor temperature cycles are generally higher in thermo-mechanical constant amplitude tests. Thermal recovery effects present at high temperatures decreased the maximum stress upon cooling (at T_{min}) when maximum temperatures were above 500°C for thermo-mechanical constant amplitude and block loading (Tables 7 and 8). This

behavior is specific to materials that exhibit significant thermal recovery at high temperatures. Alloys tailored for high temperature resistance should operate at temperatures below this regime.

3.1.3 Surface Oxide Structure

Surface oxide structure in (a) isothermal strain cycling tests, (b) thermo-mechanical fatigue tests, and (c) isothermal and thermo-mechanical zero applied load (free expansion) tests will be described below. Oxide structure in interrupted tests will be discussed in Section 3.2. Oxide thicknesses measured on failed samples were in the range 0.05 mm to 1.0 mm depending on the temperature and time. The time of oxidation varied in the range 2 to 100 hours respectively. If the equivalent oxidation time is taken to be equal to the time to failure of the specimen, oxide thicknesses measured in thermo-mechanical tests are lower than those observed in corresponding isothermal tests. However, if the oxidation time is interpreted as the fraction of time the specimen was subjected to temperatures between 600°C and 700°C, oxide thicknesses in isothermal and thermo-mechanical tests match closely. The test time (in hours) is indicated in the subsequent figures.

After etching the oxide layers, the types of oxide present could be evaluated. In isothermal tests, oxide layers larger than 10 μm have been observed only above 400°C (t_{ox} > 2 hours). The oxide layers for all isothermal tests are stratified and contain large proportions of Fe_3O_4. A schematic of a stratified oxide layer is shown in Fig. 9. Buckled sections of oxide are present at the oxide/air interface with occasional spalling of these sections observed. The majority of the

oxide layer is made up of stratifications with some accompanying porosity. Numerous short, tightly closed oxide cracks which do not extend completely through the oxide layer are observed. Stratified oxide layers exhibit wide, semi-circular oxide intrusions. An example of a stratified oxide layer observed in isothermal loading is shown in Fig. 10. The specimens were sectioned parallel to the loading direction as indicated in Fig. 10.

Thermo-mechanical constant amplitude tests exhibit stratified oxide layers (shown schematically in Fig. 9) in the case of high mean temperatures (T_{mean} > 400°C), with mostly Fe_3O_4 present (Fig. 11). When the mean temperature is lower (T_{mean} < 400°C), the oxide layer is non-stratified (FeO and Fe_3O_4) as shown schematically in Fig. 12. These oxide layers exhibit some small amount of porosities, but no stratifications are observed. Oxide intrusions are long and thin as opposed to the wide intrusions observed in stratified oxide layers. Oxide cracks are open and extend completely through the oxide layer to the metal. An example of a non-stratified oxide layer is shown in Fig. 13. Etching of the oxide and metal did not identify any preferential intrusion growth along grain boundaries.

In thermo-mechanical block tests, oxide layers are continuous when the magnitude of the minor temperature cycle is 100°C (Fig. 14), with very few oxide cracks. When the magnitude of the minor temperature cycles is greater than 100°C fragmented oxide layers are observed (Fig. 15). Only block tests with minor temperature cycles greater than 100°C exhibit extensive oxide intrusion formation.

Oxide cracks and oxide intrusions are present in all specimens subjected to external loading in the form of fully reversed strain cycling or total constraint temperature cycling. In some cases oxide cracks and oxide intrusions exhibit a one-to-one correspondence, while in other cases the number of oxide cracks is greater than the number of oxide intrusions. Average oxide crack spacing and oxide intrusion spacing are listed in Table 9 for some of the tests performed in this study.

Tests performed under zero applied load conditions resulted in non-stratified oxide layers with no evidence of oxide cracks, oxide intrusions or oxide buckling. (Fig. 16). Oxide layers in these tests are lower in depth than oxide layers in the corresponding tests where stresses are present (due to applied strain or imposed constraint), indicating that oxide failure (in the form of buckling or fatigue cracking) does lead to accelerated oxide growth rate. No evidence of oxide buckling is observed in either test under zero load conditions.

3.1.4 Internal Oxidation and Cavity Growth

Examination of virgin material showed precipitates with average diameters of 5 μm distributed throughout the pearlite structure, in most cases situated in or near small ferrite grains of average diameter 20 μm (Fig. 17). Very small cavities (d = 1 μm) are observed in these precipitates, along with some decohesion between the iron and the precipitates. Further analysis using an x-ray attachment on the scanning electron microscope indicated the precipitates were MnS particles.

All specimens in this study exhibit some degree of cavity formation after exposure to high temperatures. In the case of specimens tested

under conditions of zero applied load, cavities with maximum diameters of 3 μm are observed inside MnS particles. No cavities larger than the precipitate size were observed in either of these tests. In isothermal strain cycling tests cavities range in size from a fraction of the precipitate size to as large as 15 μm. However, thermo-mechanical loading resulted in extensive cavity formation when non-stratified oxide layers with open oxide cracks are observed. Cavities as large as 50 μm were observed in these cases. In thermal cycling tests where oxide layers are stratified (T_{mean} >500°C), less extensive cavity formation is observed. Specimens subjected to thermo-mechanical block loading exhibited pronounced cavitation when fragmented oxides (Fig. 15) are observed. Auger analysis of a failed sample revealed oxide formation inside cavities (Fig. 18).

3.2 Interrupted Tests

In an effort to better understand the progression of surface oxidation and internal cavity growth under thermal loading, two series of interrupted tests were performed. The first series of tests were isothermal constant amplitude tests at 600°C with a strain amplitude of 0.0035 and a strain rate of 0.0002 sec^{-1}. Specimens were cycled to 10 percent and 40 percent of the fatigue life. Oxide formation and oxide buckling are observed at 10 percent of the fatigue life, as shown in Fig. 19. At 40 percent of the life, a stratified oxide layer with closed oxide cracks is already observed (Fig. 19(b)). After failure, the oxide is quite thick with extensive stratification and multiple oxide cracks. The oxide layer at 100 percent of life for this case is

shown in Fig. 10. Oxide thickness, oxide intrusion depth, and crack length are shown as a function of fatigue life fraction (and time) in Fig. 20 and Table 10. Under isothermal loading, oxide cracks do not correspond directly to cracks in the metal substrate. The definitions of oxide thickness (h_o), oxide intrusion depth (h_i), and crack length (a), applicable to isothermal loading are shown in Fig. 21. While oxide intrusions begin to form at about 10 percent of the life, cracks in the metal substrate do not form until sometime after 40 percent of the life. The failure crack in the specimen tested to 100 percent of the fatigue life initiated at the tip of an oxide intrusion, but no other significant cracks in the metal substrate were observed.

Cavity size at each portion of the life is shown in Table 10. While cavity formation is observed at 10 percent of the life, at 40 percent of the life cavity diameters are still only a fraction of the MnS particle size. After failure, cavity diameters are 15 μm, which is slightly smaller than the ferrite grain size (20 μm).

The second series of interrupted tests consisted of thermo-mechanical constant amplitude loading where the temperature was cycled between 150°C and 600°C with an average strain rate on the order of 0.0002 sec^{-1}. Tests were performed to 10, 20, 30, 40, and 60 percents of fatigue life. Oxide structure is continuous during all portions of the life (Fig. 22), with oxide cracks and oxide intrusions present as early as 10 percent of the life (Fig. 22(a)). Unlike isothermal behavior, oxide cracks under thermo-mechanical loading continue directly into the metal substrate even before 10 percent of the fatigue life. Oxide thickness, oxide intrusion depth, and crack length are identified

in Fig. 23 and are shown as a function of fatigue life fraction (and time) in Fig. 24 and Table 11. Crack growth is accompanied by intrusion growth up to about 60 percent of the life. After 60 percent of the life, cracks grow at a faster rate than oxide intrusions and eventually lead to failure. Initial oxide growth is approximately linear with subsequent growth following a parabolic curve. Oxide growth is slower under thermo-mechanical loading than under isothermal loading since specimens are only subjected to high temperatures during a portion of the thermal cycle.

Furthermore, it is interesting to note that the growth rates of small cracks (as shown in Fig. 24) and the accompanying intrusions are very high. Crack growth rate decreases as the cracks grow longer (during the middle portion of the fatigue life), with high growth rates again observed late in the life (Fig. 24). Crack growth rate of small cracks in interrupted isothermal tests is much lower (Fig. 20) than that observed under thermo-mechanical loading.

Cavity formation and growth for thermo-mechanical interrupted tests are shown in Fig. 25 and Table 11. Internal oxidation and cavity formation are seen as early as 10 percent of the life (3 hours) as shown in Fig. 25(b). At 40 percent of the life, internal oxidation is pronounced (Fig. 25(d)). Figures 25(e) and 25(f) show the progression of internal oxidation and cavity growth with time, and upon closer examination it is quite evident that oxide formation has occurred in cavities at 60 percent and at 100 percent of the life.

4. DISCUSSION

4.1 Oxide Characteristics (IF versus TMF)

All specimens in this study which experienced temperatures of 500°C or greater exhibited significant oxide formation. Since oxidation in steels can accelerate crack initiation, comparisons of oxide structure and characteristics for various loading conditions can provide insight into the differing mechanisms of damage that may develop. Compressive stresses can lead to buckling of oxide layers and subsequent stratification if new oxide layers form under the buckled sections [35,36]. Factors which may influence oxide stresses include Pilling-Bedworth Ratio, thermal expansion coefficient mismatch between oxide and metal, and mechanical strains in the form of isothermal strain cycling or temperature cycling under constraint.

The effects of oxide growth stresses and thermal expansion coefficient mismatch stresses on oxide structure in the absence of externally applied loading were explored in tests performed under zero applied load conditions. The oxide layers observed in these tests exhibited non-stratified oxide layers with no evidence of oxide cracks, oxide intrusions, or oxide buckling (Fig. 16). This indicates that oxide growth stresses and thermal expansion coefficient mismatch stresses are not sufficient to cause oxide failure in the absence of external loading.

When externally applied loading is considered, either in the form of fully reversed isothermal strain cycling or totally constrained thermo-mechanical cycling, oxide failure does occur. Extensive oxide cracking perpendicular to the applied loading direction (Mode I), and in

some cases oxide buckling and stratification parallel to the applied strain direction are the main failure features observed in the oxides. Often the oxide is assumed to behave elastically up to failure, axial oxide stresses would then be linearly related to axial oxide strains.

Isothermal loading does not involve any temperature variation so oxide constraint temperature and thermal expansion coefficient mismatch do not affect oxide strains in these tests. However, external loading in the form of strain cycling is imposed on the oxide. Approximate oxide strains which develop during typical isothermal tests are shown are Figs. 26 and 27. The oxide strains represented in Figs. 26 and 27 do not include those due to oxide growth, which would be similar for isothermal and thermo-mechanical loading. Oxide mean strains are zero in both cases since all isothermal tests were performed under fully reversed strain cycling. Oxide structure in these tests is stratified with oxide crack flanks fully closed. These cracks become non-propagating as they approach the oxide-metal interface. Extensive oxide buckling has occurred in these cases upon loading into compression (Fig. 10). In isothermal loading cases, crack growth begins after 40 percent of the life and initiates at the tip of an oxide intrusion.

Under thermo-mechanical loading, oxide constraint temperature and thermal expansion coefficient mismatch dictate the sign and magnitude of oxide stresses. The oxide strains which develop in two particular thermo-mechanical tests (shown as dashed lines) are illustrated in Figs. 26 and 27. In strain calculations, the coefficient of thermal expansion of the oxide (Fe_3O_4) is assumed to be approximately twice that of steel between 470°C and 610°C [34], while outside this regime it matches the

expansion coefficient of steel (1.7×10^{-5}/°C). The solid lines represent oxide strains in comparable isothermal tests (described above) where the mechanical strain ranges in the metal for both types of loading are the same and the isothermal tests are performed at the maximum thermo-mechanical temperature. The oxide is assumed to be constrained at 500°C since most oxide forms at higher temperatures while the metal is constrained at the minimum thermo-mechanical temperature. The constraint temperature for the oxide was chosen mainly for qualitative comparison in Figs. 26 and 27, while actual behavior is probably somewhat more complicated (with strain variation across the oxide thickness). Oxide cracks which remain open during the cycle lead to cracks in the metal substrate as early as 10% of the fatigue life. This may accelerate damage in the metal substrate to a greater extent than stratified oxide layers with closed oxide cracks (typically observed in isothermal cases). Experimental results of tensile and compressive loadings on iron oxides reported in the literature [30] show a relatively low strain to fracture in tension (0.0004), while that in compression is about a factor of three higher. Therefore, oxide cracking may occur more readily in thermo-mechanical loading cases considered in this study.

When the mean temperature in thermo-mechanical loading is above 400°C (Fig. 26), the axial oxide strain is similar in isothermal and thermo-mechanical cases. Oxide mean strains are near zero or compressive in these cases. This results in an oxide layer which is stratified with closed (non-propagating) oxide cracks (Fig. 11). Similar to the isothermal cases discussed above, extensive oxide buckling has occurred in these cases.

Under thermo-mechanical block loading, oxide strains would be a combination of those shown for constant amplitude loading in Figs. 26 and 27. During the major temperature cycle, a non-stratified oxide with open (propagating) oxide cracks would form. During subsequent minor temperature cycles these layers would be subject to buckling due to low oxide mean strains associated with these cycles, allowing stratifications to form. The subsequent major temperature cycles would result in new open oxide cracks in this stratified layer, causing the fragmented oxide shown in Fig. 15. Therefore, thermo-mechanical block loading may exhibit higher oxide damage than in isothermal and/or thermo-mechanical fatigue cases.

4.2 Cavity Formation And Growth

Some level of cavity growth is seen in all specimens subjected to high temperatures in this study. If cavity growth is controlled mainly by applied stress, the most severe cavitation would be expected under high temperature isothermal loading in this study. The high tensile stresses developed in thermo-mechanical tests (Tables 7 and 8) occur at the low temperature end of the thermal cycle (Fig. 8), where creep damage is minimal. In isothermal tests, high tensile and compressive stresses both occur at high temperatures (Tables 2 through 4 and Fig. 8). While the compressive stresses may result in some recovery of cavitation creep damage [38], tensile stresses associated with these tests should result in more extensive cavitation than the stresses associated with thermo-mechanical tests. The results of this study show the most extensive cavity growth occurring under thermo-mechanical loading,

while cavitation in isothermal tests is much less extensive. Therefore some other mechanism must be the driving force behind cavity growth.

Several recent studies have considered cavity formation and growth due to chemical attack on precipitate particles in metals [40,41]. If internal chemical attack is the driving force behind cavity growth, gaseous access to the metal substrate would be an important factor when oxides are present. Cavitation should be most extensive in cases where the oxide layer is nonprotective, allowing the access of gaseous species to the metal substrate through out a major portion of the test. In this study, the most extensive cavitation is observed in thermo-mechanical constant amplitude tests which exhibit open oxide cracks and thermo-mechanical block tests where oxide is fragmented and stratified. Both of these oxides allow easy access of the atmosphere to the metal substrate. Less pronounced cavitation is observed in cases where the oxide layer may be considered partially protective, resulting in less extensive atmospheric access to the metal substrate. Examples include zero applied load tests where oxide is continuous with no oxide cracks or oxide buckling, isothermal tests where oxide is stratified but oxide cracks are tightly closed, and thermo-mechanical constant amplitude tests (high mean temperature) where oxides are stratified with closed oxide cracks. This indicates that internal chemical attack is a likely driving force for cavity growth in this study.

If chemical attack is occurring in this material, the following reactions are possible and must be considered: (a) hydrogen attack of carbon, (b) oxygen attack of carbon, (c) oxygen attack of sulfur present in MnS particles. These reactions may occur in the following forms:

(a) $Fe_3C(s) + 2H_2(g) \rightarrow 3Fe(s) + CH_4(g)$

(b) $C(s) + O_2(g) \rightarrow CO_2(g)$

(c) $C(s) + \frac{1}{2} O_2(g) \rightarrow CO(g)$

(d) $MnS(s) + \frac{1}{2} O_2(g) \rightarrow MnO(s) + \frac{1}{2} S_2(g)$

(e) $MnS(s) + \frac{3}{2} O_2(g) \rightarrow MnO(s) + SO_2(g)$

where (s) refers to a solid and (g) refers to a gas. The partial pressures of the gases produced from each of these reactions may be quite large in some cases and lead to the growth of cavities in the metal [40].

The calculations of the internal partial pressures of the gaseous products in the above reactions are shown in APPENDIX 1. The result of these calculations are shown in Table 12 for a temperature of 600°C and partial pressures of the gaseous reactants equal to the atmospheric values. It is obvious from Table 12 that reaction (a) results in the lowest partial pressure of product gas, indicating that this reaction would be the least likely driving force behind cavity growth. Of the remaining four reactions, (b) and (d) result in the highest partial pressures of product gases and so would be most likely to cause cavity growth. The pressures listed for all four of the oxygen reactions are too high to realistically be expected in an internal cavity. This is a result of the fact that calculations in APPENDIX 1 assume equilibrium conditions. If the solubility of oxygen in Fe is too low to allow these reactions at equilibrium rates, the values of partial pressure for the product gases would be greatly reduced. It was found in Ref. 51 that

the solubility of oxygen in Fe at 600°C is quite low, indicating that actual values of partial gas pressures would be several orders of magnitude or more lower than those listed in Table 12.

Another factor which could influence the reactions listed above would be the rate of diffusion of oxygen into the metal substrate. The rate of lattice diffusion, D, of oxygen in Fe can be calculated at any temperature using the following equation,

$$D = D_o \exp(-Q/kT), \qquad (1)$$

where D_o is the diffusivity constant and Q is the activation energy. For the diffusion of oxygen in Fe, a diffusivity constant of 3.7×10^{-12} cm^2/sec, and an activation energy of 23.2 kcal/mol were used [51]. Substituting these values into Eq. (1) results in a diffusion rate of 6.16×10^{-8} cm^2/sec at 600°C.

To calculate the time required for oxygen to diffuse completely to interior of the specimens used in this study, the following equation may be used,

$$t = x^2/2D, \qquad (2)$$

where t is the time required for oxygen to diffuse to a distance x. At 600°C, the time required for oxygen to diffuse through the lattice to the center of a specimen (x = 0.38 cm) would be greater than 350 hours. This is significantly longer than the longest test in this study. However, if grain boundary diffusion occurs, diffusion rates

could be as much as four orders of magnitude faster [52]. Therefore complete oxygen diffusion along grain boundaries could occur in a matter of minutes as opposed to days. Lattice diffusion would then be required to move oxygen from the grain boundaries to the center of the grains. If Eq. (2) is once again used with the distance x equal to one half the ferrite grain size (x = 10 μm), the resulting diffusion time would be less than 10 seconds. This indicates that complete diffusion of oxygen to all areas of the specimen is possible shortly after the start of a test.

Using the information stated above, oxygen could be present through out the material shortly after the start of a test, leading to internal oxidation, probably in the form of reaction (b) or (d). It is most likely that the reaction of oxygen with sulfur occurs first since small cavities in the MnS particles and some particle decohesion was seen in virgin material (Fig. 17). These small holes would act as potential sites for the nucleation of reaction (d) since sulfur is readily available. However, after the cavity size exceeds the MnS particle size, the reaction of oxygen with carbon could also readily occur. Evidence of this mechanism is shown in Fig. 28 for cavity growth in the interrupted thermo-mechanical tests. Up to about 35 percent of the life, cavities grow slowly inside the MnS particles, with limited oxygen solubility and oxygen diffusion rate having some effect on the reaction rate. After 35 percent of the life, the rate of growth increases as cavities grow through the proeutectoid ferrite and the pearlite.

5. CONCLUSIONS

1. Oxide structure is dependent on temperature and strain. Consequently, isothermal and thermo-mechanical loading cases result in differing oxide structures even when applied mechanical strains and strain rates in the metal are similar for both cases.

   a. Oxides formed under zero applied load conditions experience oxide strains which are not high enough to cause buckling or cracking of the oxide.

   b. Oxides formed under fully reversed isothermal strain cycling experience reversed oxide strains with oxide mean strains approximately zero. Oxide structure is stratified, with extensive oxide buckling throughout the layer. Oxide cracks grow perpendicular to the applied strains and become nonpropagating as they approach the oxide/metal interface.

   c. Oxides formed during total constraint thermo-mechanical fatigue where $T_{mean} > 400°C$ experience reversed oxide strains with oxide mean strains near zero. Oxide structure is similar to that observed under isothermal loading, with stratified oxide layers and closed oxide cracks that do not propagate into the metal substrate.

   d. Oxides formed during total constraint thermo-mechanical fatigue where $T_{mean} < 400°C$ experience reversed oxide strains with mean tensile oxide strains. Oxide structure in this case is relatively nonstratified with (open) oxide cracks that propagate into the metal substrate early in the life.

2. Internal cavities form by oxygen attack of MnS precipitate particles. Cavity growth is accelerated due to high partial pressures of product gases which develop in the cavities. This mechanism is pronounced in cases where oxide layers are non-protective (open (propagating) oxide cracks) since the partial pressure of oxygen at the metal/oxide interface approaches the atmospheric value.

3. The mechanism of surface and internal oxidation driven crack nucleation and growth is likely to be present in the tread and flange regions of railroad wheels, and would explain the large number of fatigue cracks observed in service.

4. Further experiments are needed where isothermal fatigue and thermomechanical fatigue under the absence of environment effects are examined. This would allow a realistic assessment of the contribution of oxidation to crack nucleation and growth.

Table 1 Chemical Composition of Class U Wheel Steel

C	Mn	Si	Cn	Cr	P	S	Ni	Mo
0.64	0.8	0.2	0.08	0.06	<0.05	0.047	0.03	<0.02

Table 2 Isothermal Constant Amplitude Fatigue Test Results $\dot{\varepsilon} = 0.02\ sec^{-1}$

a) T = 20°C

$\Delta\varepsilon/2$	$\Delta\sigma/2$ (MPa)	N_f (cycles)
0.0015	344	1.30×10^6
0.0020	360	55102
0.0025	386	24046
0.0035	413	5503

b) T = 200°C

$\Delta\varepsilon/2$	$\Delta\sigma/2$ (MPa)	N_f(cycles)
0.0015	298	1.0×10^6
0.0020	375	196483
0.0025	385	27686
0.0035	454	11189

c) T = 400°C

$\Delta\varepsilon/2$	$\Delta\sigma/2$ (MPa)	N_f(cycles)
0.0015	285	1.71×10^6
0.0020	318	40354
0.0025	377	8502
0.0035	413	6262

d) T = 600°C

$\Delta\varepsilon/2$	$\Delta\sigma/2$ (MPa)	N_f(cycles)
0.0015	173	27166
0.0020	165	7748
0.0025	219	6054
0.0035	255	2631

e) T = 700°C

$\Delta\varepsilon/2$	$\Delta\sigma/2$ (MPa)	N_f(cycles)
0.0015	108	21486
0.0020	123	9633
0.0035	106	5629

Table 3 Isothermal Constant Amplitude Fatigue Test Results $\dot{\varepsilon} = 0.002\ sec^{-1}$.

a) T = 20°C

$\Delta\varepsilon/2$	$\Delta\sigma/2$ (MPa)	N_f(cycles)
0.005	459	2796
0.010	485	84

b) T = 100°C

$\Delta\varepsilon/2$	$\Delta\sigma/2$ (MPa)	N_f(cycles)
0.010	568	245

c) T = 200°C

$\Delta\varepsilon/2$	$\Delta\sigma/2$ (MPa)	N_f(cycles)
0.005	542	2081
0.010	690	125

d) T = 300°C

$\Delta\varepsilon/2$	$\Delta\sigma/2$ (MPa)	N_f(cycles)
0.010	728	89

e) T = 400°C

$\Delta\varepsilon/2$	$\Delta\sigma/2$ (MPa)	N_f(cycles)
0.002	307	19046
0.005	480	2323
0.010	566	309

f) T = 500°C

$\Delta\varepsilon/2$	$\Delta\sigma/2$ (MPa)	N_f(cycles)
0.010	448	188

Table 3 (Continued)

g) T = 600°C

$\Delta\varepsilon/2$	$\Delta\sigma/2$ (MPa)	N_f(cycles)
0.002	168	4190
0.005	264	822
0.010	292	156

h) T = 700°C

$\Delta\varepsilon/2$	$\Delta\sigma/2$ (MPa)	N_f(cycles)
0.0035	94	2392
0.002	142	942
0.010	143	283

Table 4 Isothermal Constant Amplitude Fatigue Test Results $\dot{\varepsilon} = 0.0002\ sec^{-1}$

a) T = 400°C

$\Delta\varepsilon/2$	$\Delta\sigma/2$ (MPa)	N_f(cycles)
0.0020	282	21000
0.0035	359	1474
0.0050	407	1370

b) T = 600°C

$\Delta\varepsilon/2$	$\Delta\sigma/2$ (MPa)	N_f(cycles)
0.0020	127	1286
0.0035	155	700
0.0050	105	228

c) T = 700°C

$\Delta\varepsilon/2$	$\Delta\sigma/2$ (MPa)	N_f(cycles)
0.0020	62	2600
0.0035	70	1028
0.0050	72	617

Table 5 Strain-Life Equation Constants for 1070 Steel $\dot{\varepsilon} = 0.02\ sec^{-1}$

T(°C)	E(MPa)	b	c	ε_f'	σ_f' (MPa)
20	200860	-0.093	-0.464	0.0996	958
200	198280	-0.095	-0.466	0.1005	1173
400	189340	-0.121	-0.630	0.4310	1255
600	145200	-0.141	-0.516	0.1575	647

Table 6 Strain-Life Equation Constants for 1070 Steel $\dot{\varepsilon} = 0.0002\ sec^{-1}$

T(°C)	E(MPa)	b	c	ε_f'	σ_f' (MPa)
400	189340	-0.114	-0.526	0.1426	936
600	145200	-0.004	-0.659	0.2583	112
700	116640	-0.062	-0.752	0.9359	98

Table 7 Thermo-Mechanical Constant Amplitude Fatigue Test Results $\dot{\varepsilon}_{av} = 0.0002\ sec^{-1}$

Temperature Range (°C)	Mechanical Strain $\Delta\varepsilon_m$	σ_{max} (MPa)	$\Delta\sigma$ (MPa)	N_f (Cycles)
150-450	0.0051	538	771	3048
150-500	0.0060	550	745	1524
150-600	0.0076	526	681	735
150-650	0.0085	517	668	436
150-650	0.0085	522	674	573
150-700	0.0094	477	659	410
400-600	0.0034	358	465	2537
400-700	0.0051	354	449	1099
500-600	0.0017	188	264	10709
500-650	0.0026	245	335	2010
500-700	0.0034	250	334	1271
550-650	0.0026	131	177	13287

Table 8 Thermo-Mechanical Block Loading Fatigue Tests Results $\dot{\varepsilon}_{av} = 0.0002\ sec^{-1}$

a) Major Temperature Range = 150°C - 500°C

Minor Temperature Range	B_f (Blocks)	Major Cycles σ_{max} (MPa)	Major Cycles $\Delta\sigma$ (MPa)	Minor Cycles σ_{max} (MPa)	Minor Cycles $\Delta\sigma$ (MPa)
400°C - 500°C	325 +	545	744	174	296
350°C - 500°C	86	525	715	309	472
300°C - 500°C	68	545	739	394	562

+ no failure occurred

b) Major Temperature Range = 150°C - 600°C

Minor Temperature Range	B_f (Blocks)	Major Cycles σ_{max} (MPa)	Major Cycles $\Delta\sigma$ (MPa)	Minor Cycles σ_{max} (MPa)	Minor Cycles $\Delta\sigma$ (MPa)
500°C-600°C	144	484	661	160	250
450°C-600°C	62	508	654	252	354
400°C-600°C	21	531	676	330	447

Table 8 (Continued)

c) Major Temperature Range = 150°C - 650°C

Minor Temperature Range	B_f (Blocks)	Major Cycles σ_{max} (MPa)	Major Cycles $\Delta\sigma$ (MPa)	Minor Cycles σ_{max} (MPa)	Minor Cycles $\Delta\sigma$ (MPa)
550°C - 650°C	92	516	672	151	224
500°C - 650°C	38	526	676	220	305
450°C - 650°C	19	521	663	311	402

d) Major Temperature Range = 150°C - 700°C

Minor Temperature Range	B_f (Blocks)	Major Cycles σ_{max} (MPa)	Major Cycles $\Delta\sigma$ (MPa)	Minor Cycles σ_{max} (MPa)	Minor Cycles $\Delta\sigma$ (MPa)
600°C - 700°C	69	436	590	108	162

Table 9 Average Oxide Crack Spacing and Oxide Intrusion Spacing

a) Thermo-Mechanical Constant Amplitude Loading

Temperature Range °C	Mechanical Strain $\Delta\varepsilon_m$	Oxide Crack Spacing (mm)	Oxide Intrusion Spacing (mm)
150 - 500	0.0060	0.05	0.05
150 - 600	0.0076	0.10	0.10
150 - 650	0.0085	0.13	0.13
150 - 700	0.0094	0.24	0.24
500 - 600	0.0017	0.47	1.0
550 - 650	0.0017	1.0	1.0

b) Isothermal Constant Amplitude Loading

Temperature (°C)	Mechanical Strain $\Delta\varepsilon_m$	Oxide Crack Spacing (mm)	Oxide Intrusion Spacing (mm)
600	0.0070	0.20	0.35

Table 10 Oxide Thickness, Intrusion Depth and Cavity Diameter for Interrupted Isothermal Constant Amplitude Tests
$T = 600°C$, $\Delta\varepsilon_m = 0.0070$, $\dot{\varepsilon} = 0.0002\ sec^{-1}$

N (Cycles)	$\frac{N}{N_f}$	Time (hours)	Oxide Thickness (μm)	Intrusion Depth (μm)	Cavity Size (μm)
70	0.10	1.5	35	40	<5
280	0.40	6.0	150	210	<5
700	1.00	15.0	550	800	15

Table 11 Oxide Thickness, Intrusion Depth and Cavity Diameter for Interrupted Thermo-Mechanical Constant Amplitude Tests, T = 150°C - 600°C

N (Cycles)	$\frac{N}{N_f}$	Time (hours)	Oxide Thickness (μm)	Intrusion Depth (μm)	Cavity Diameter (μm)
75	0.10	3	15	3	3
100	0.20	6	21	17	4
225	0.30	9	16	21	4
300	0.40	12	35	40	15
450	0.60	18	40	80	30
735	1.00	30	50	230	50

Table 12 Partial Gas Pressures

Reaction	Partial Gas Pressure
(a)	$P_{CH_4} = 7.4 \times 10^{7}$ MPa
(b)	$P_{CO_2} = 6.0 \times 10^{21}$ MPa
(c)	$P_{CO} = 6.7 \times 10^{9}$ MPa
(d)	$P_{S_2} = 1.9 \times 10^{11}$ MPa
(e)	$P_{SO_2} = 1.7 \times 10^{22}$ MPa

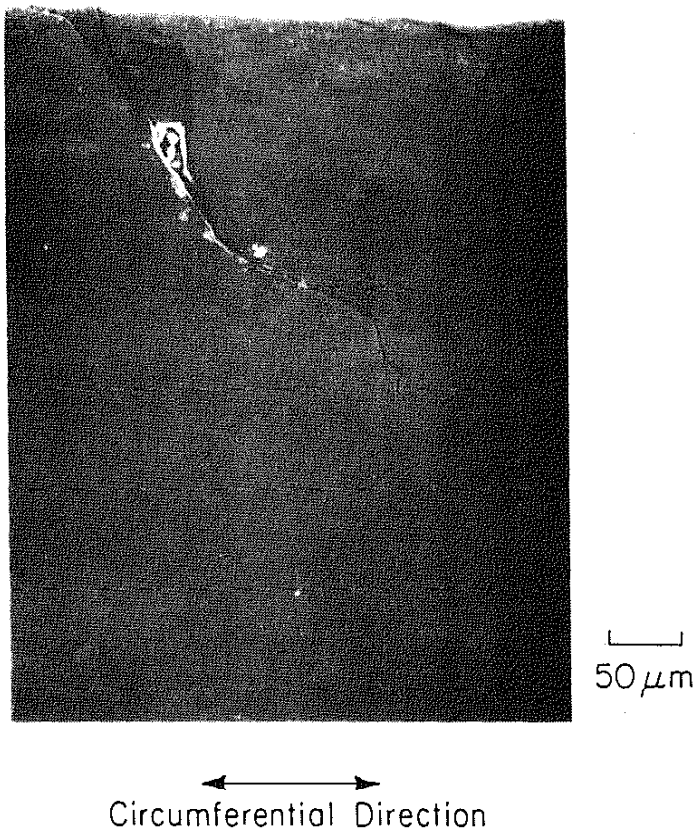

Figure 1 Oxide Penetration and Crack Growth into Railroad Wheel Tread

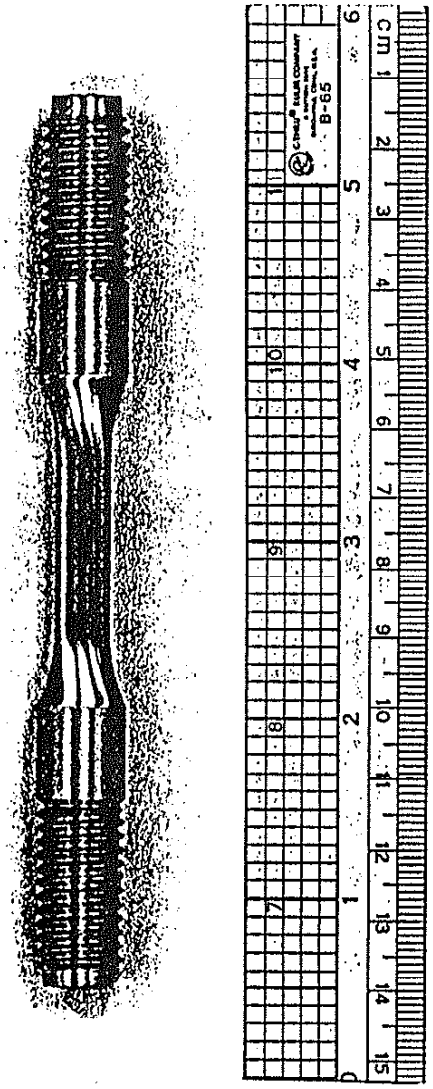

Figure 2 Uniaxial Test Specimen

Figure 3 Typical Microstructure of 1070 Steel

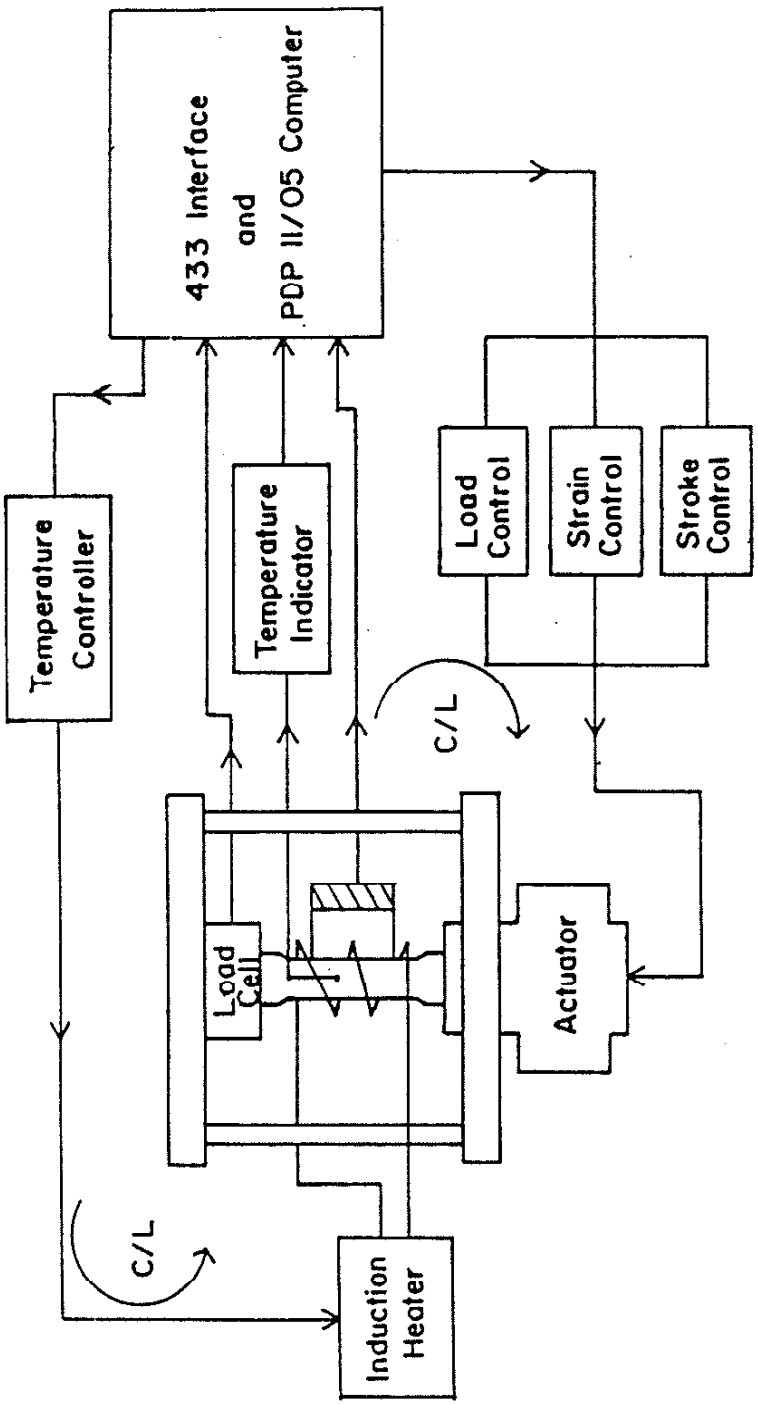

Figure 4 Schematic of Test System

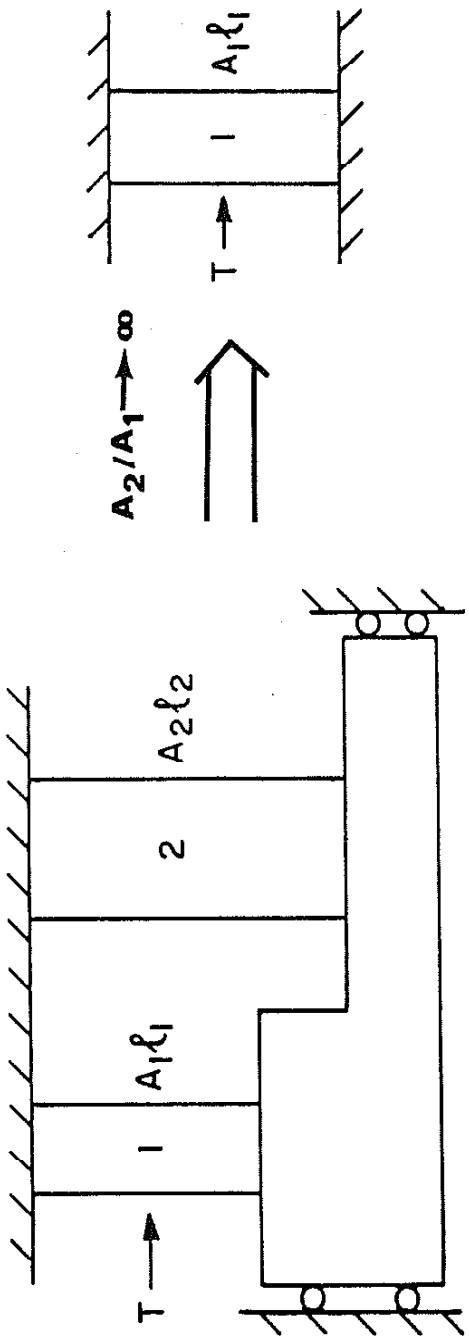

Figure 5 Parallel Bar Model and the Case of Total Constraint

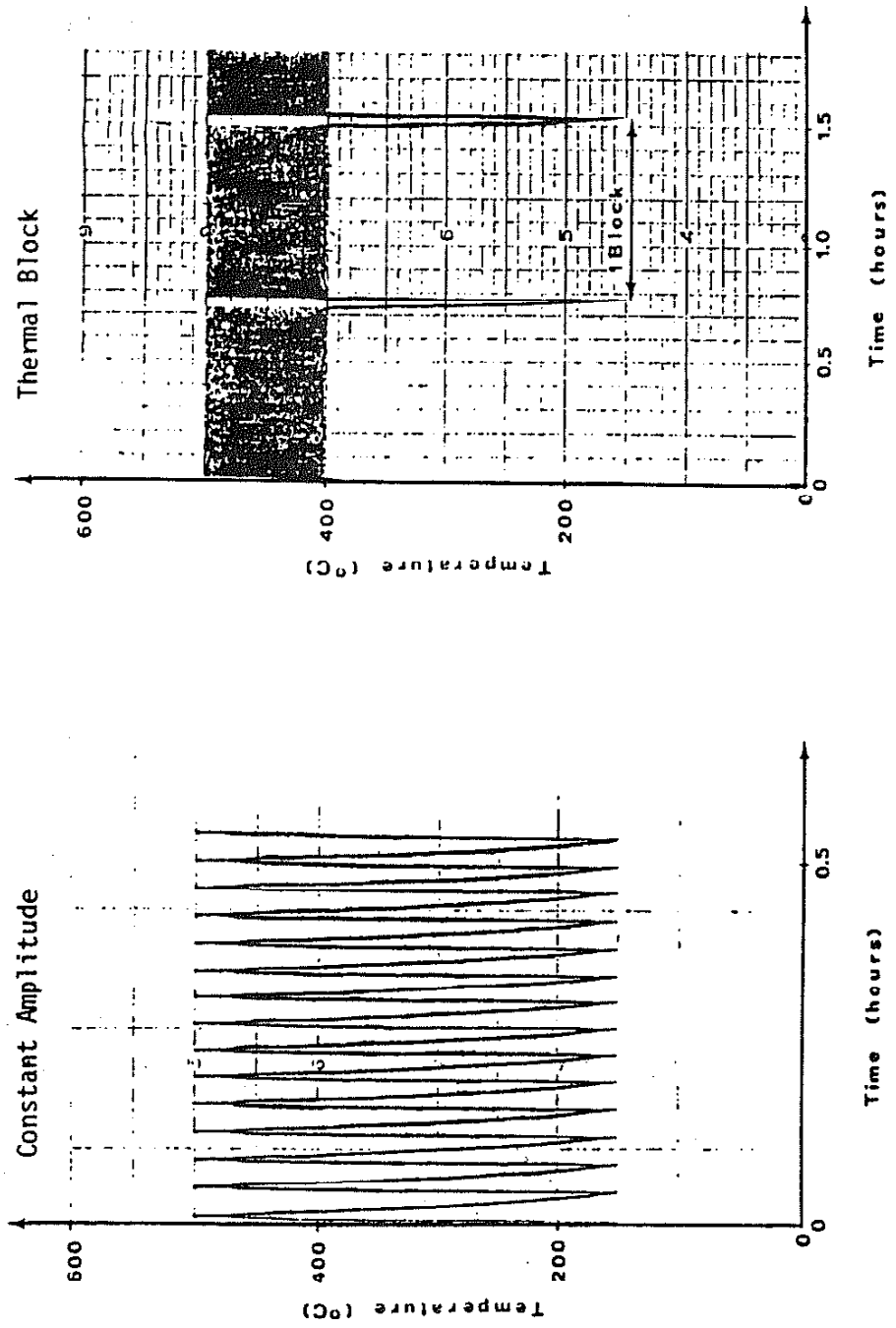

Figure 6 Experimental Temperature-Time Histories for Thermo-Mechanical Loading

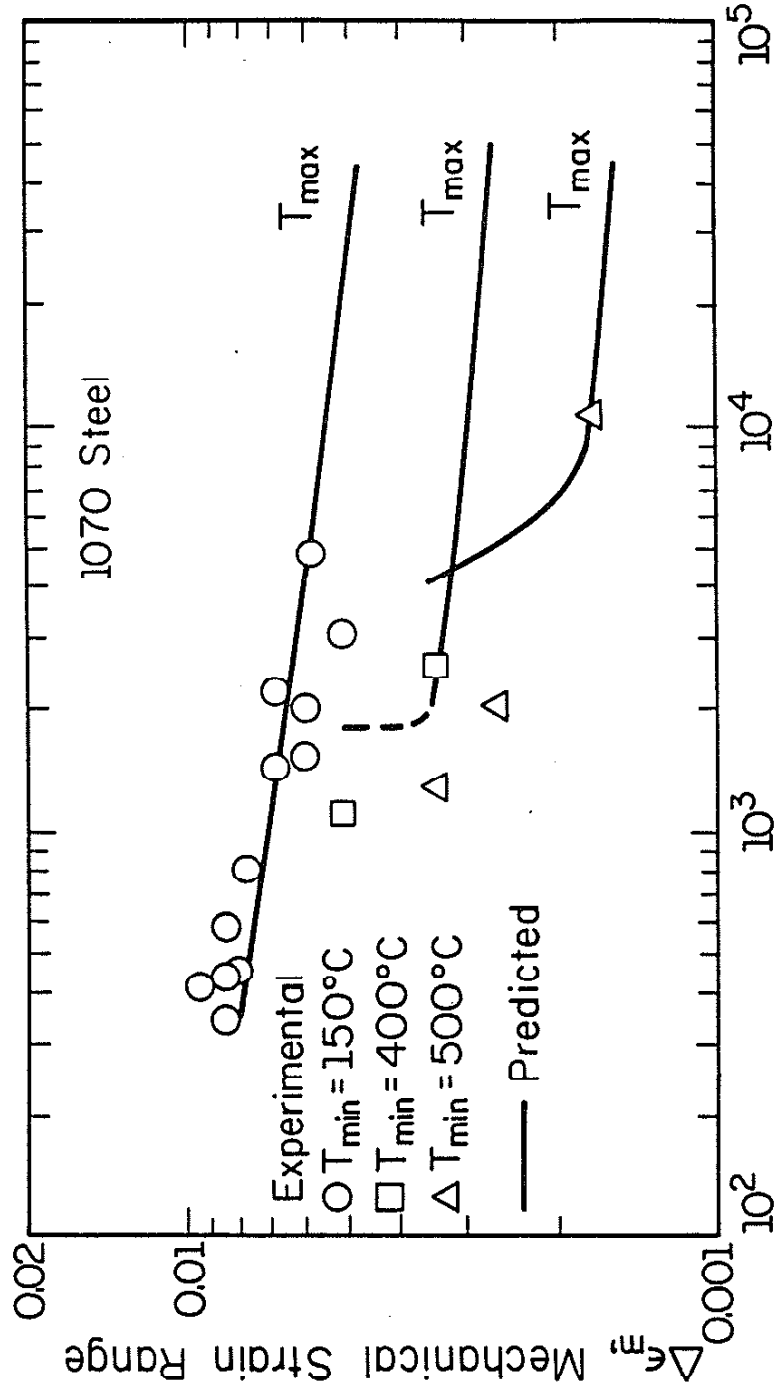

Figure 7 Predictions of Thermo-Mechanical Constant Amplitude Lives Based on Isothermal (T_{max}) Data

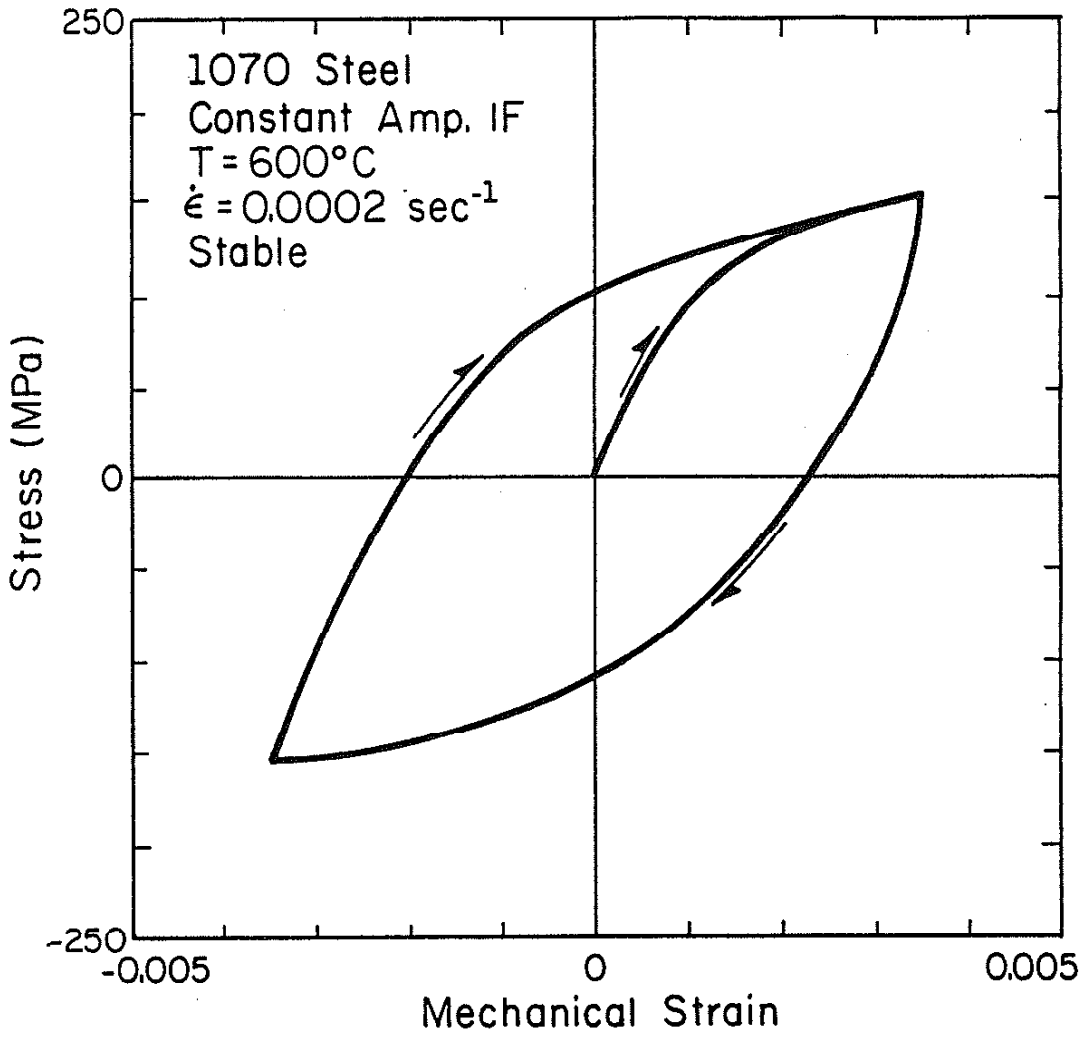

(a) Isothermal Fatigue

Figure 8 Typical Material Response

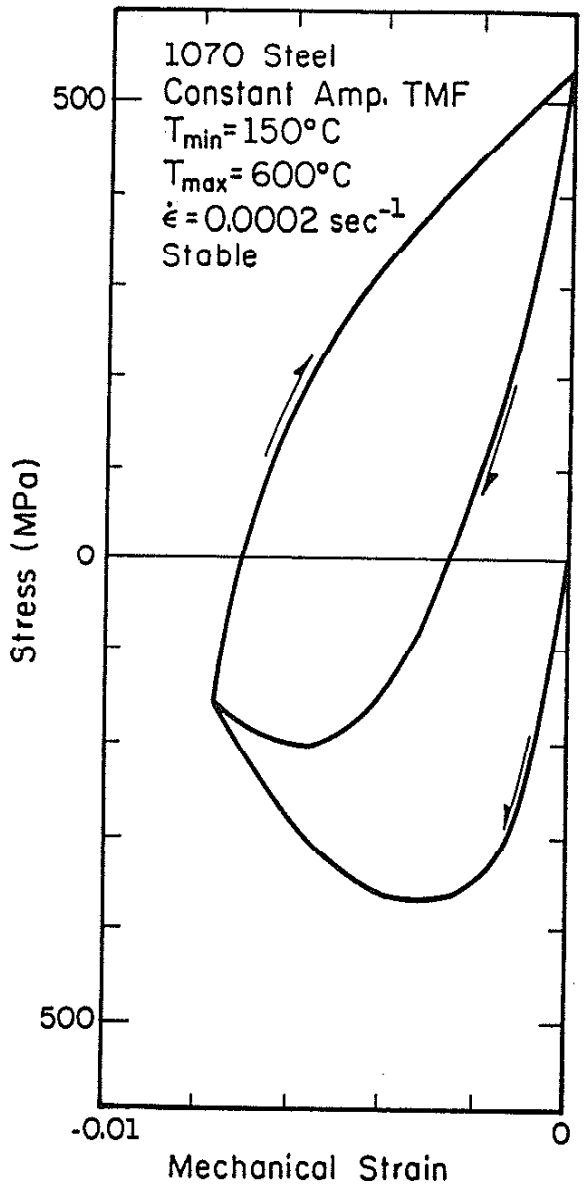

(b) Thermo-Mechanical Fatigue

Figure 8 (continued)

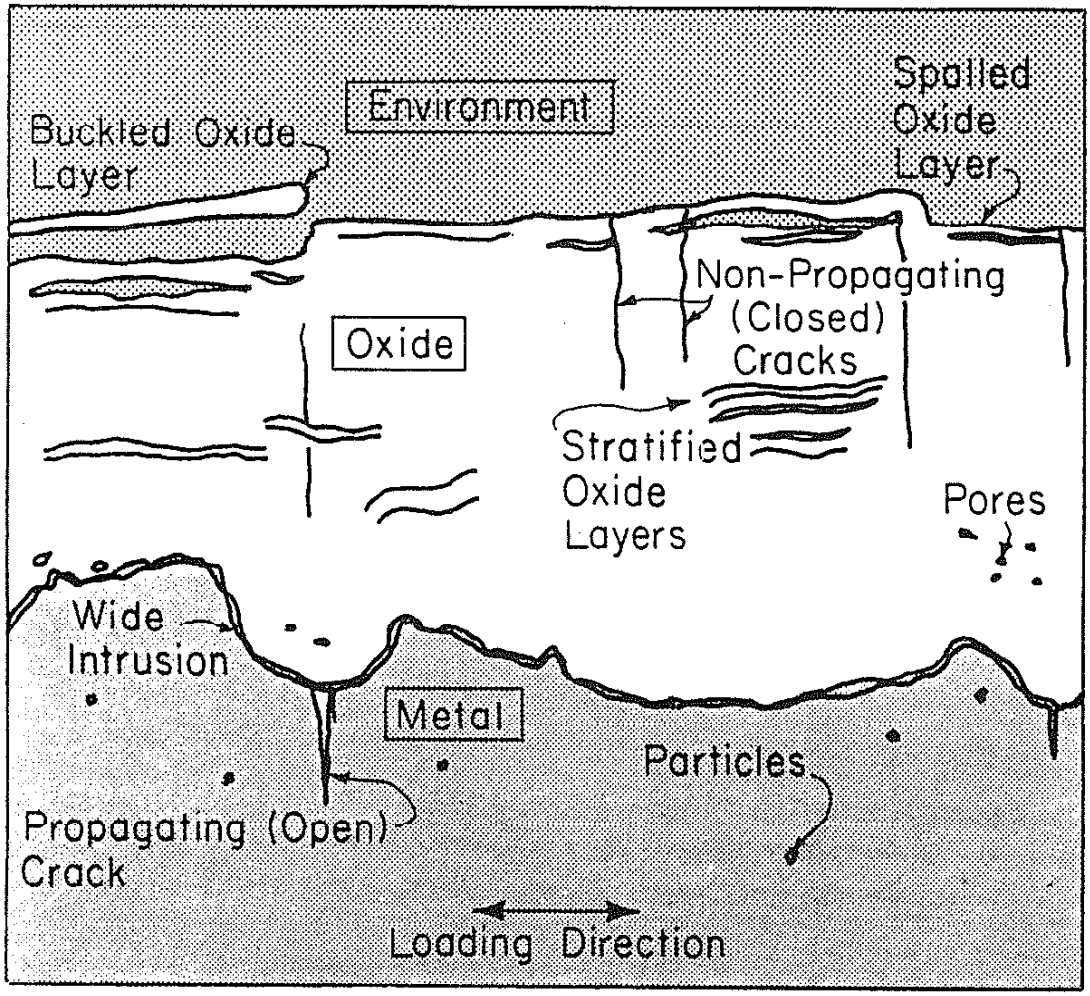

Figure 9 Schematic of Stratified Oxide Layer

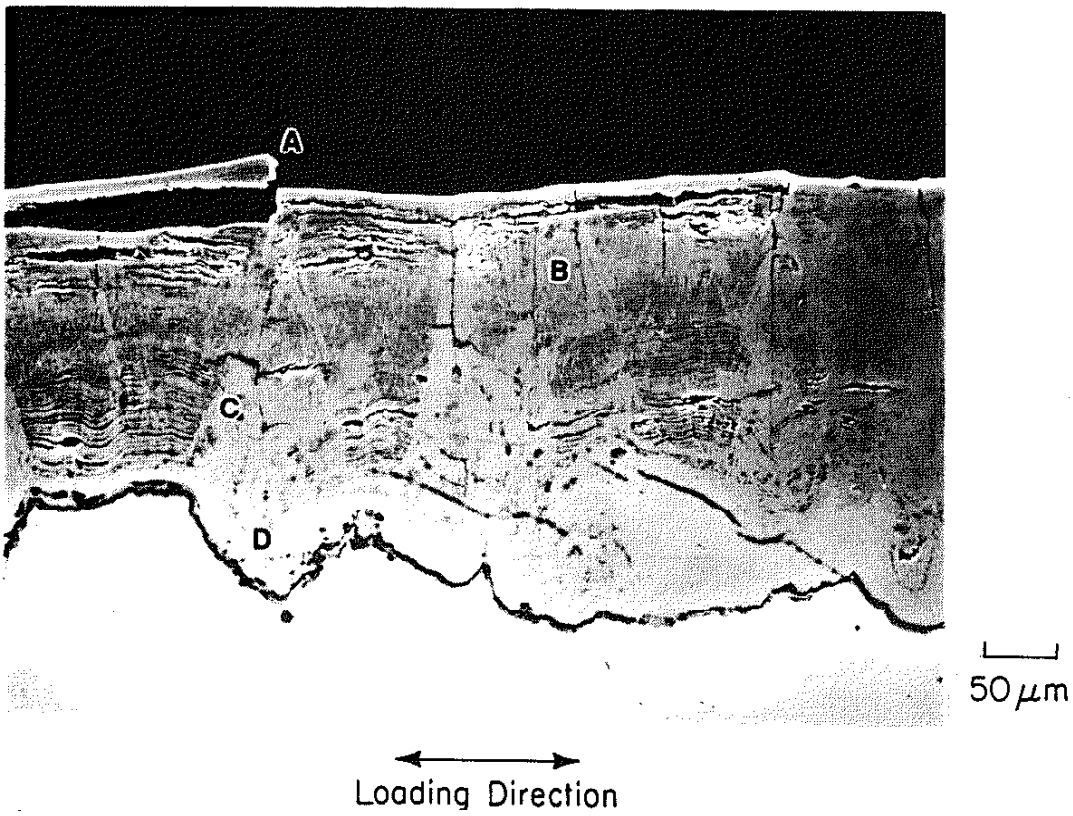

A. Buckled Oxide Layer

B. Non-propagating Oxide Cracks

C. Stratified Oxide Layers

D. Wide Oxide Intrusion

Figure 10 Stratified Oxide Layer Observed in Isothermal Constant Amplitude Loading, $\bar{T}$ = 600°C, $\Delta\varepsilon$ = 0.0070, $\dot{\varepsilon}$ = 0.0002 sec^{-1}, Test time = 16 hours

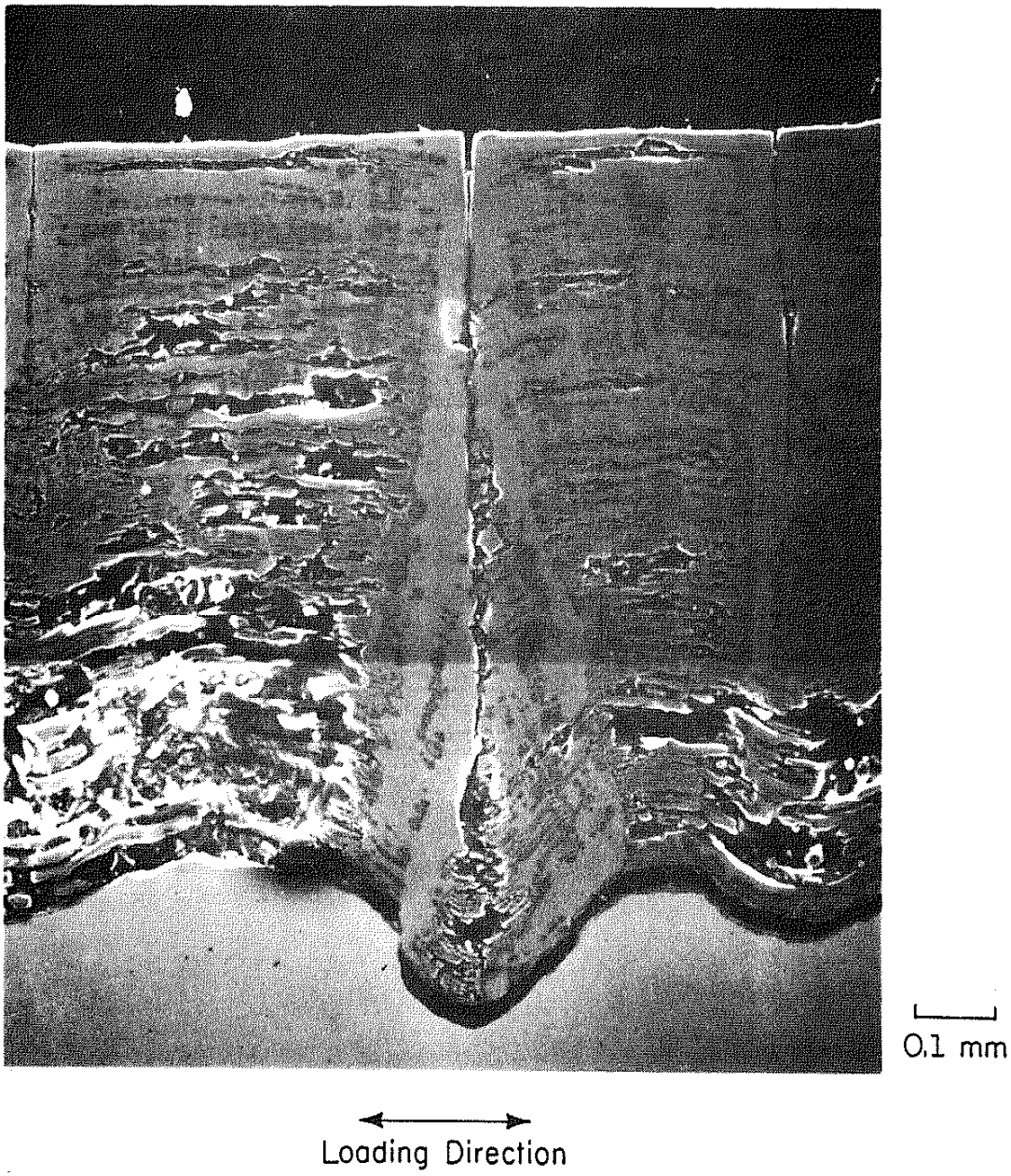

Figure 11 Stratified Oxide Layer Observed in Thermo-Mechanical Constant Amplitude Loading with T_{mean} > 400°C, T_{min} = 500°C, T_{max} = 600°C, Test time = 98 hours

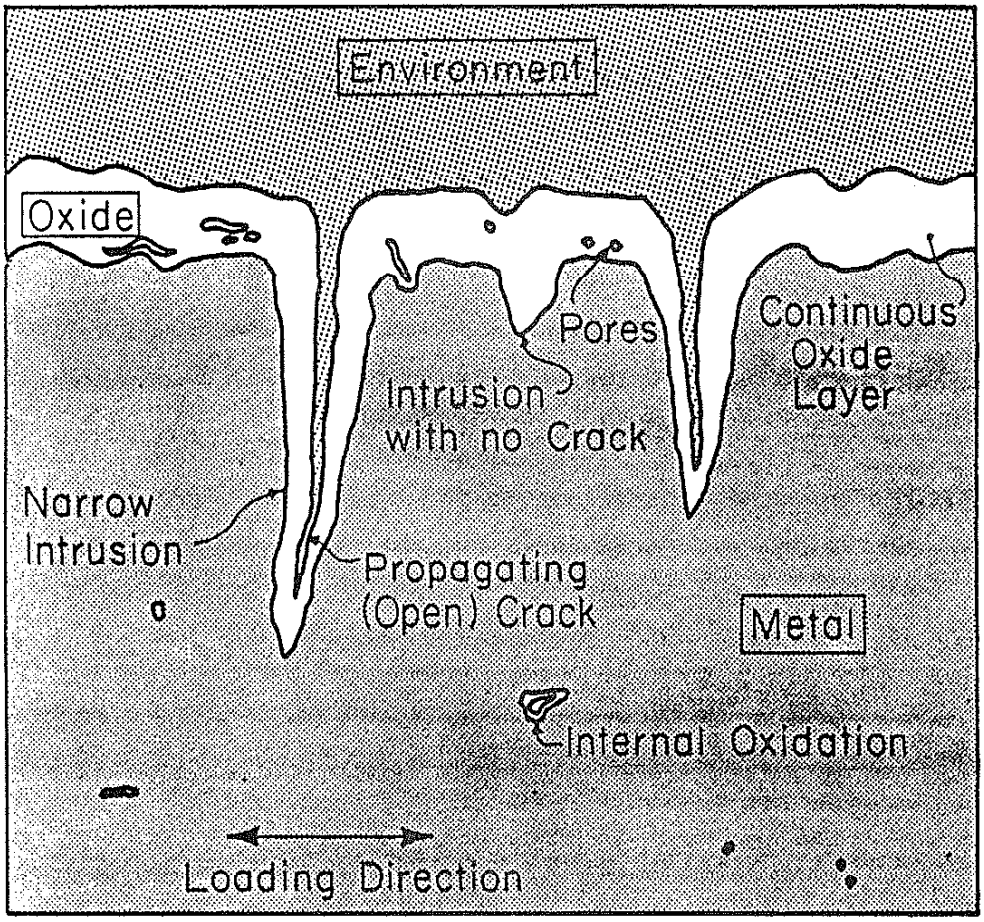

Figure 12 Schematic of Non-Stratified Oxide Layer

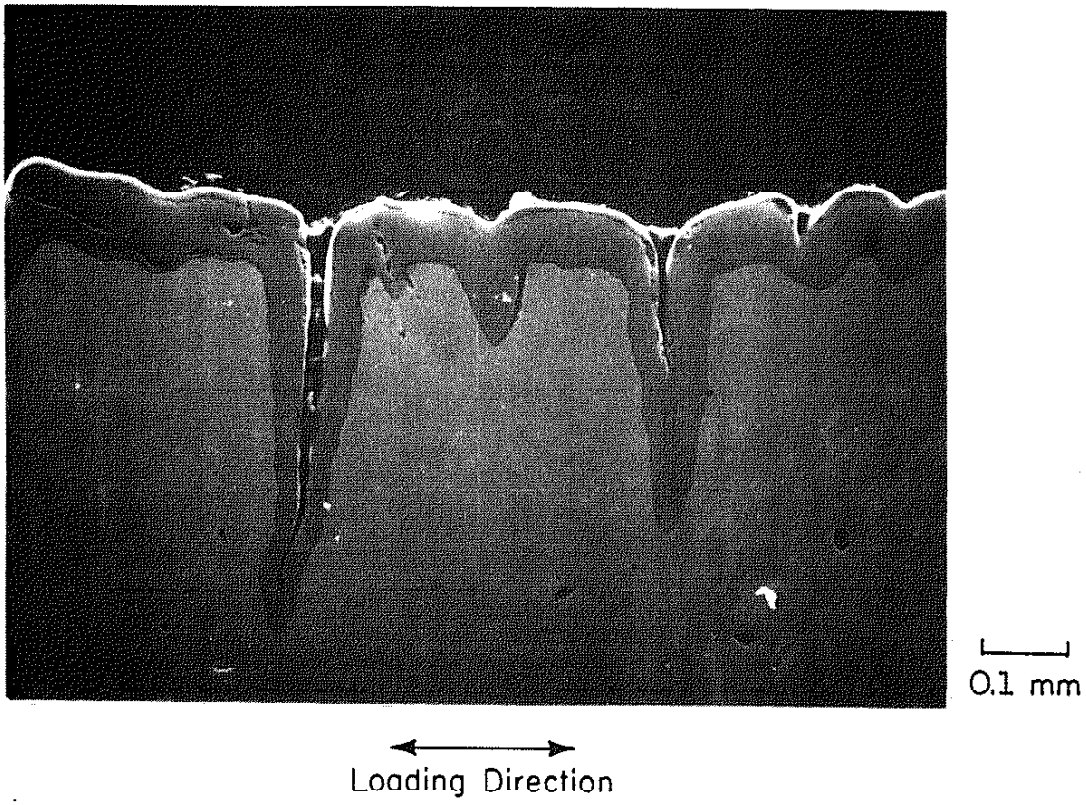

Figure 13 Non-Stratified Oxide Layer Observed in Thermo-Mechanical Constant Amplitude Loading with $T_{mean} < 400°C$, $T_{min} = 150°C$, $T_{max} = 600°C$, Test time = 30 hours

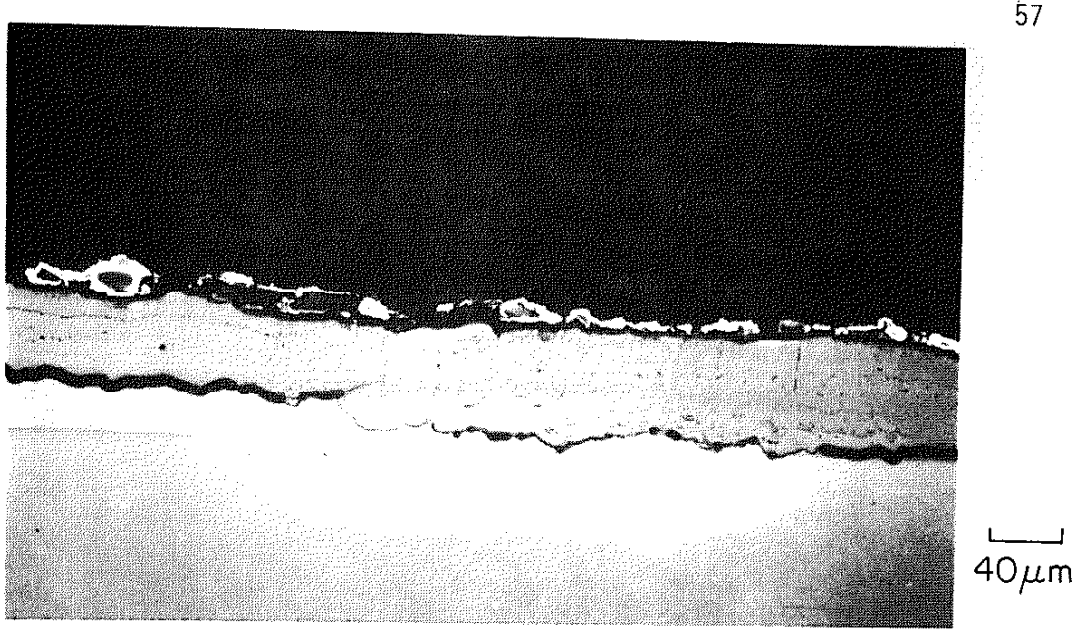

(a) Major Temperature Cycle: T_{min} = 150°C, T_{max} = 600°C
Minor Temperature Cycles: T_{min} = 500°C, T_{max} = 600°C

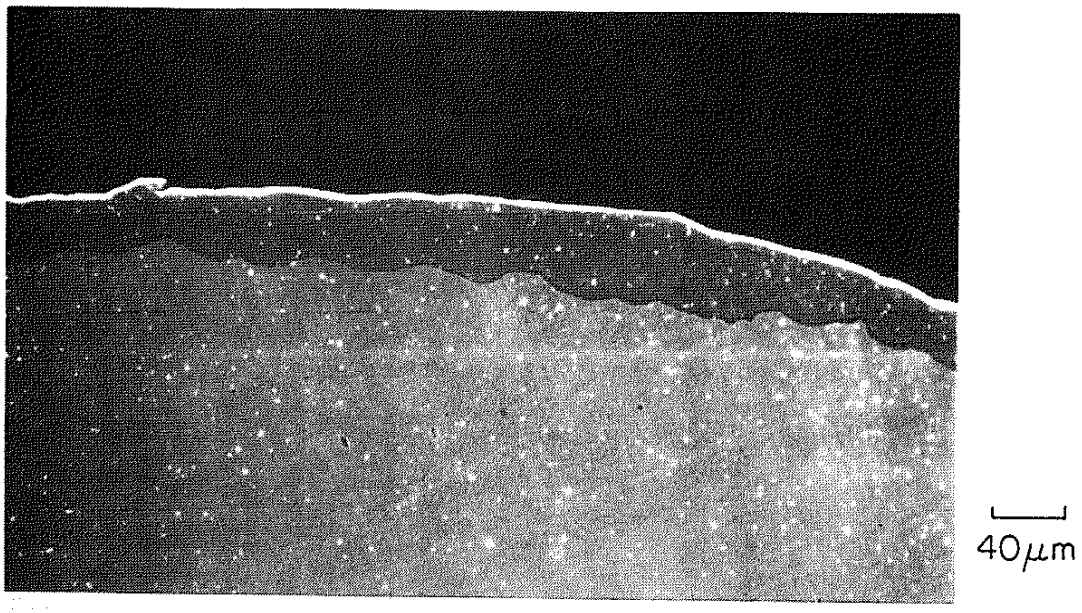

(b) Major Temperature Cycle: T_{min} = 150°C, T_{max} = 650°C
Minor Temperature Cycles: T_{min} = 550°C, T_{max} = 650°C

Figure 14 Non-Stratified Oxide Layers Observed in Thermo-Mechanical Block Loading with ΔT_{minor} = 100°C

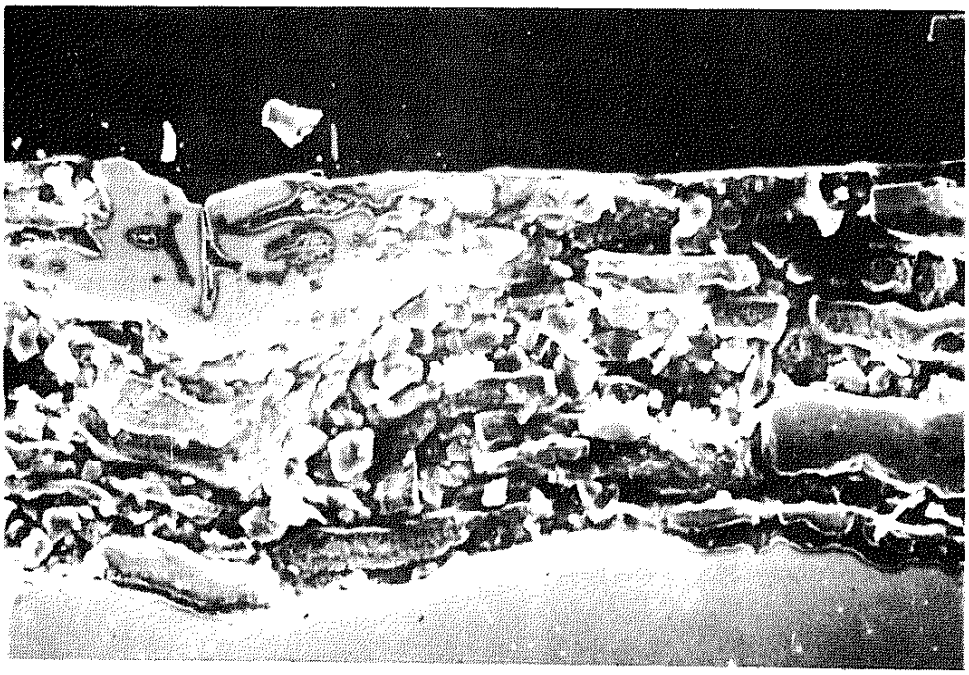

(a) Major Temperature Cycle: T_{min} = 150°C, T_{max} = 650°C
Minor Temperature Cycles: T_{min} = 500°C, T_{max} = 650°C

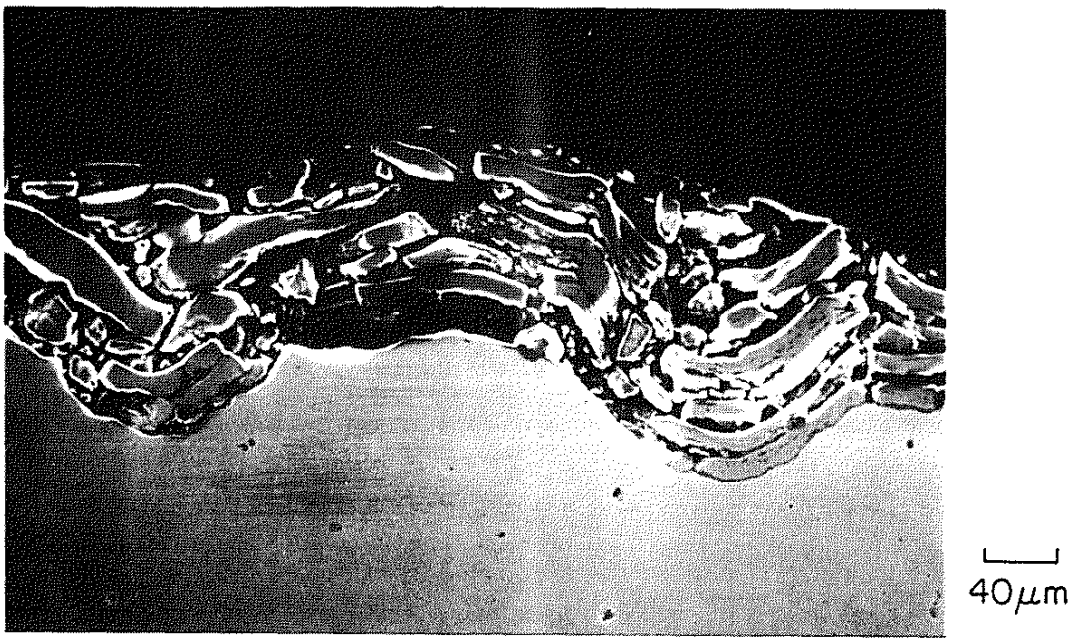

(b) Major Temperature Cycle: T_{min} = 150°C, T_{max} = 650°C
Minor Temperature Cycles: T_{min} = 450°C, T_{max} = 650°C

Figure 15 Fragmented Oxide Layers Observed in Thermo-Mechanical Block Loading with $\Delta T_{minor} > 100°C$

(a) Isothermal Zero Applied Load Test
T = 600°C, Test time = 16 hours

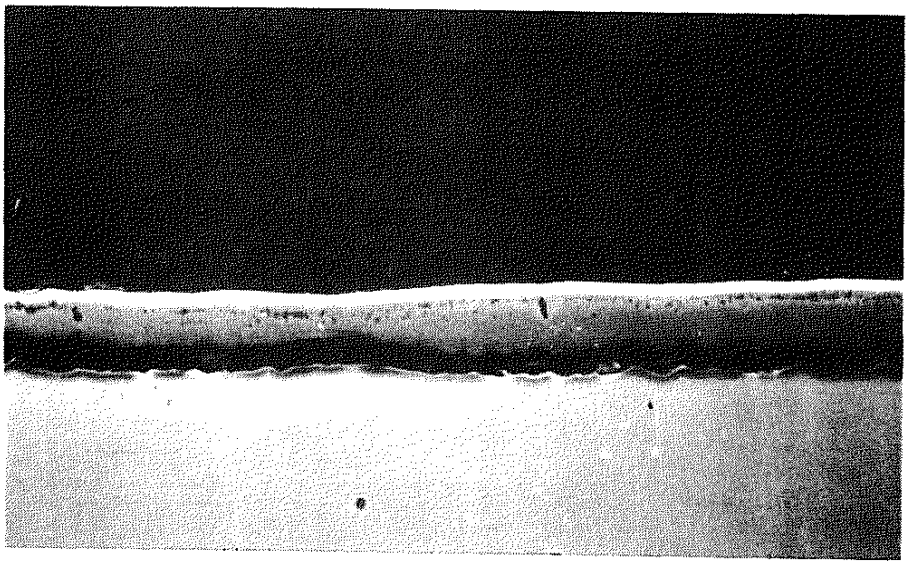

(b) Thermal Cycling Zero Applied Load Test
T_{min} = 150°C, T_{max} = 600°C, Test time = 30 hours

Figure 16 Non-Stratified Oxide Layers Observed in Zero Applied Load Tests

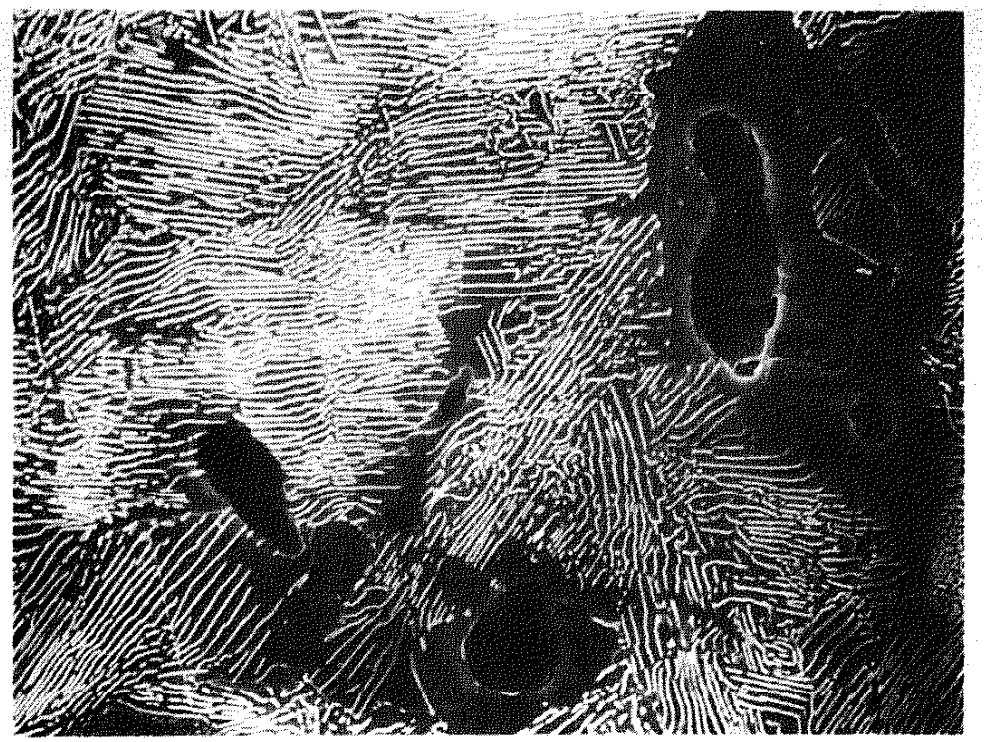

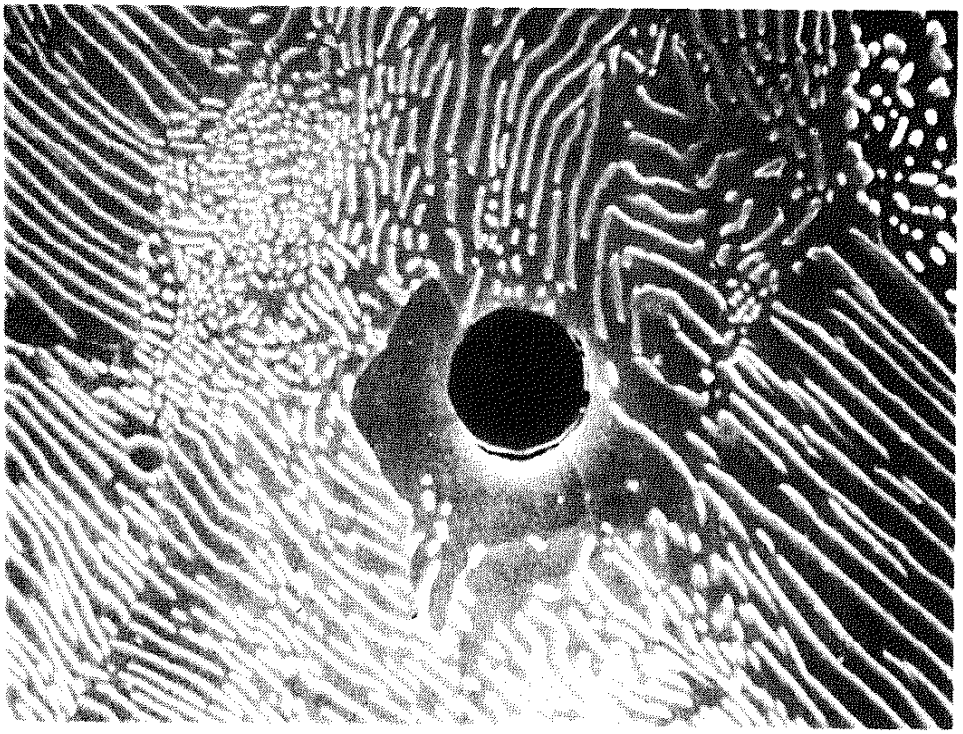

Figure 17 MnS Precipitate Particles Surrounded by Ferrite Grains in 1070 Steel

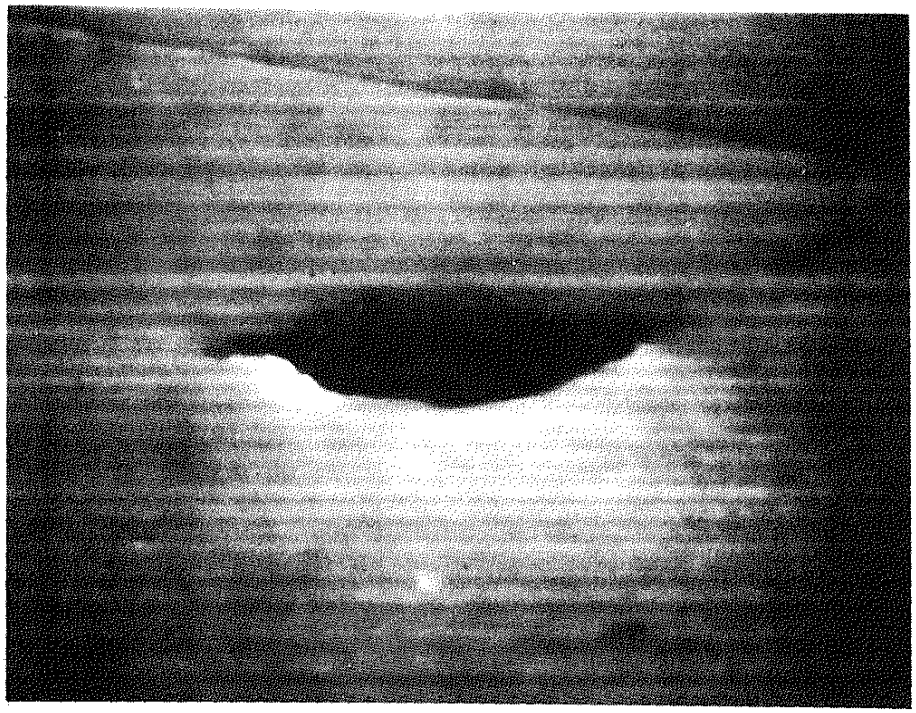

(a) SEM Photograph of Cavity

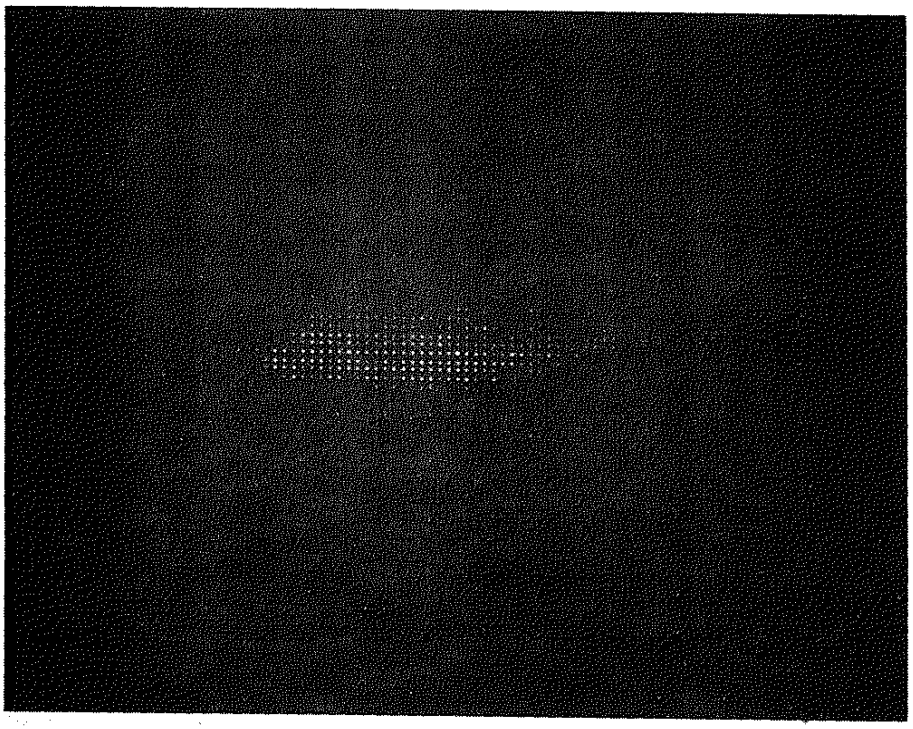

(b) Oxygen Map of Cavity Area

Figure 18 Oxide Formation in Cavity

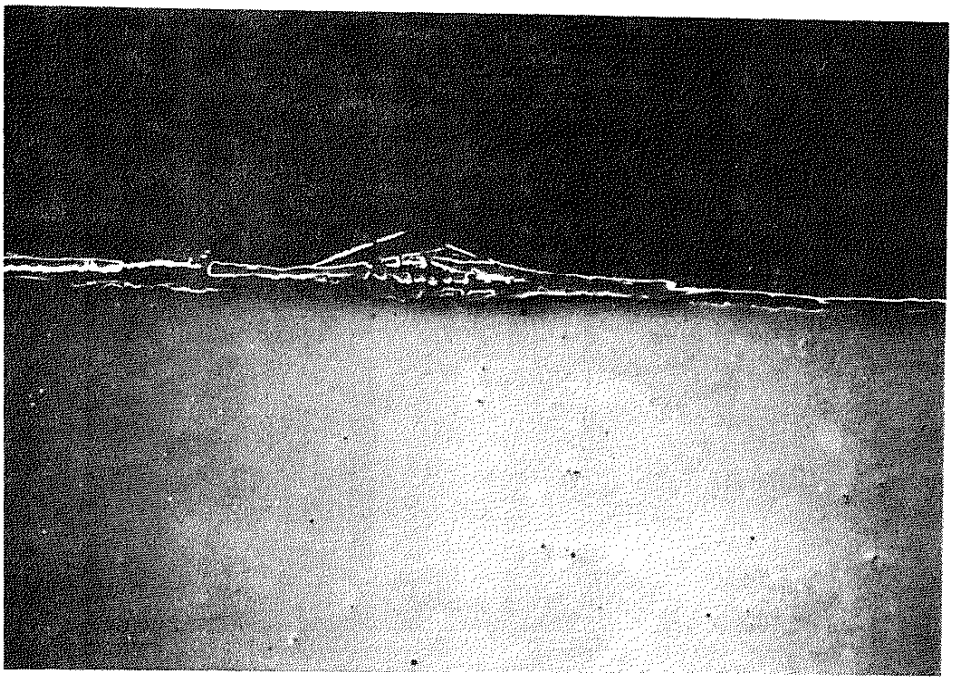

(a) 10 percent of life, Test time = 1.5 hours

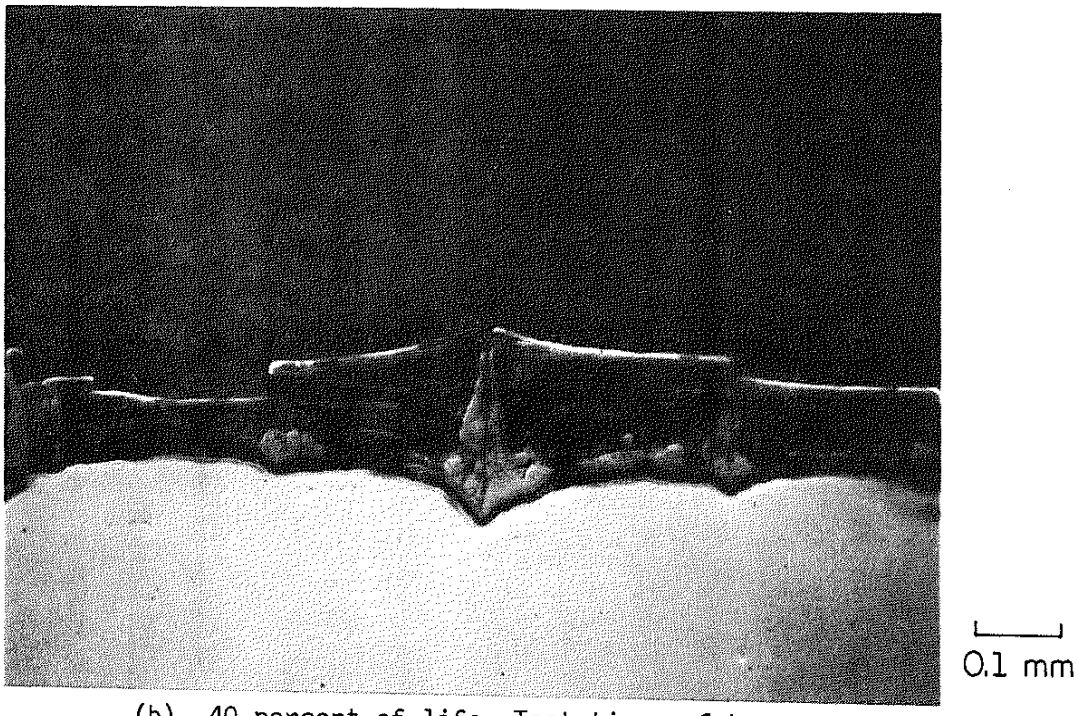

(b) 40 percent of life, Test time = 6 hours

Figure 19 Oxide Growth During Interrupted Isothermal Fatigue Tests, T = 600°C, $\Delta\varepsilon$ = 0.0070, $\dot{\varepsilon}$ = 0.0002 sec^{-1}

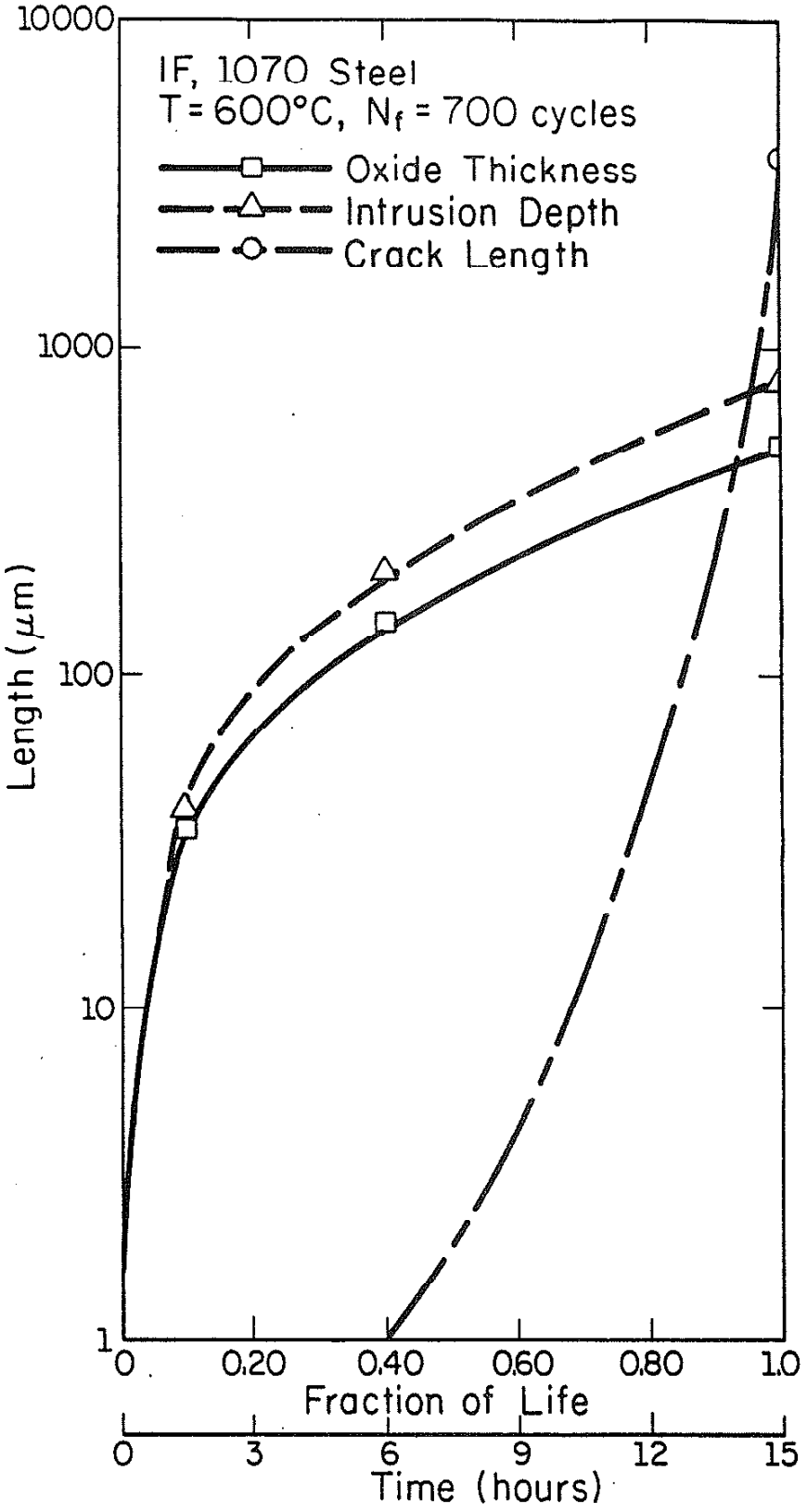

Figure 20 Oxide Thickness (h_o), Oxide Intrusion Depth (h_i), and Crack Length (a) During Isothermal Fatigue Tests, T = 600°C, $\Delta\varepsilon$ = 0.0070, $\dot{\varepsilon}$ = 0.0002 sec^{-1}

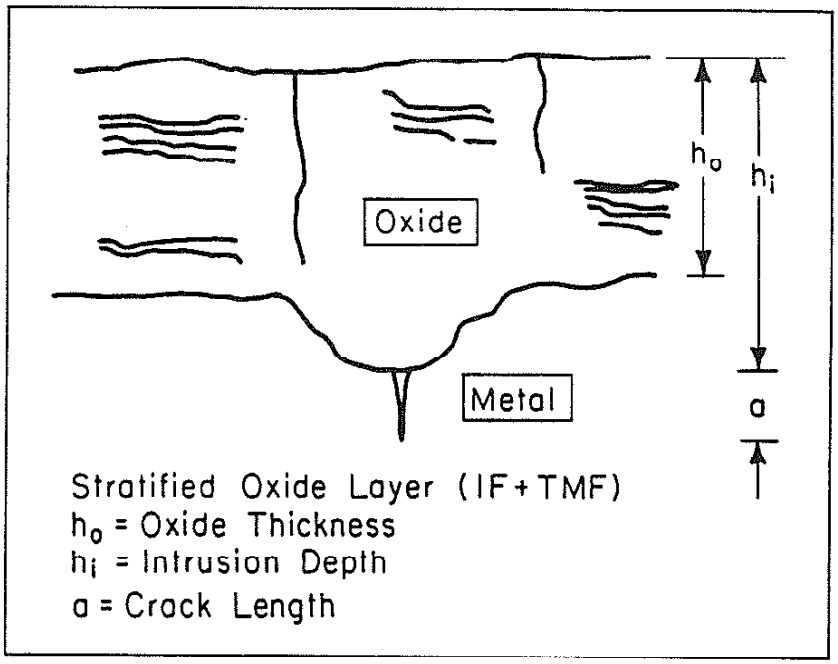

Figure 21 Definitions of h_o, h_i, and a for Stratified Oxide Layers

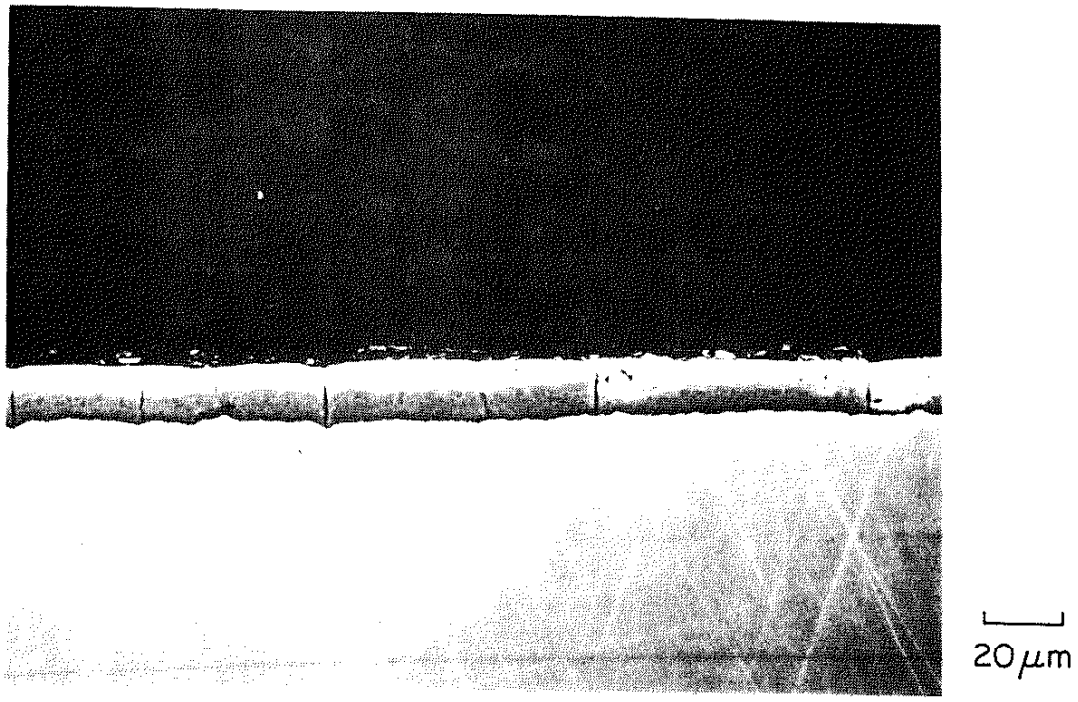

(a) 10 percent of life, Test time = 3 hours

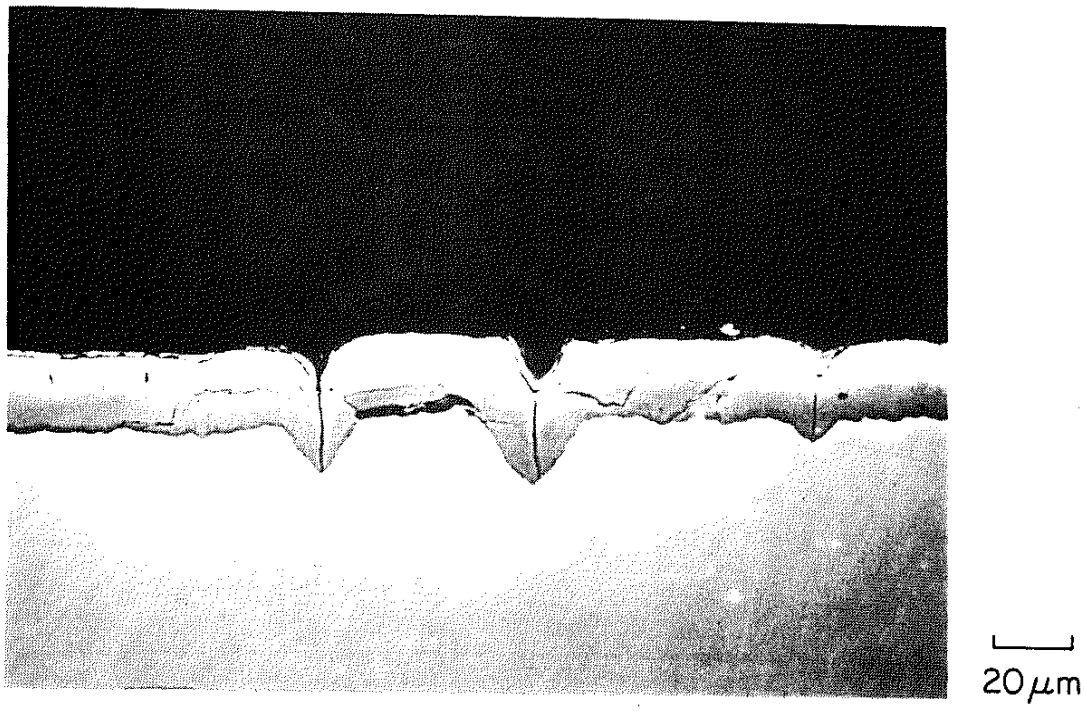

(b) 20 percent of life, Test time = 6 hours

Figure 22 Oxide Growth During Thermo-Mechanical Fatigue Tests, T_{min} = 150°C, T_{max} = 600°C, $\dot{\varepsilon}_{av}$ = 0.0002 sec^{-1}

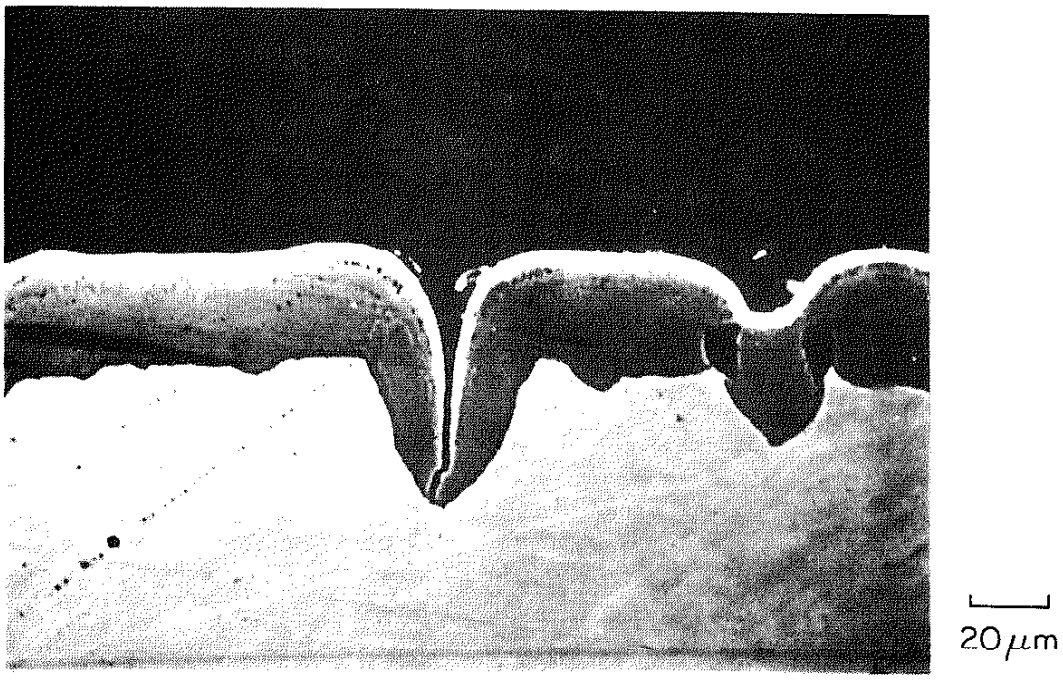

(c) 40 percent of life, Test time = 12 hours

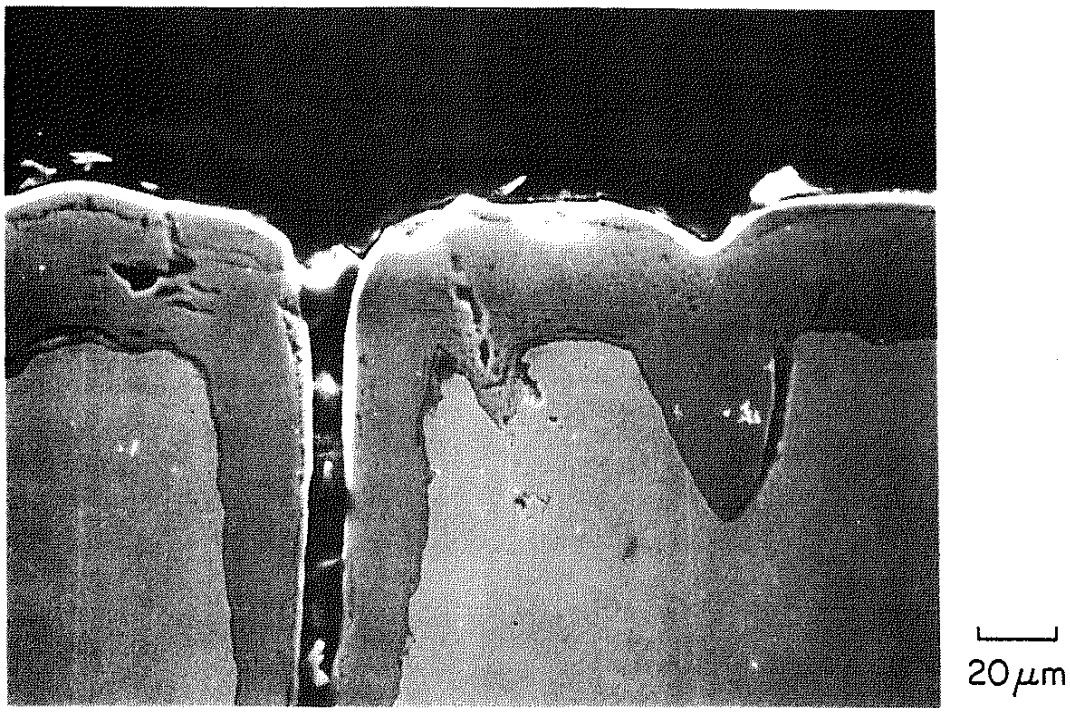

(d) 100 percent of life, Test time = 30 hours

Figure 22 (continued)

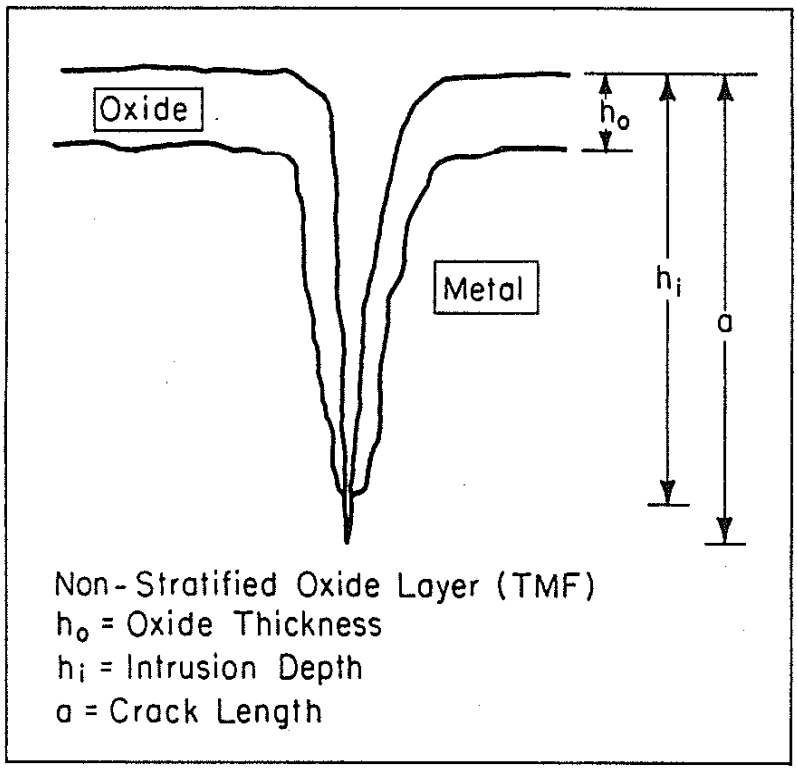

Figure 23 Definitions of h_o, h_i, and a for Non-Stratified Oxide Layers

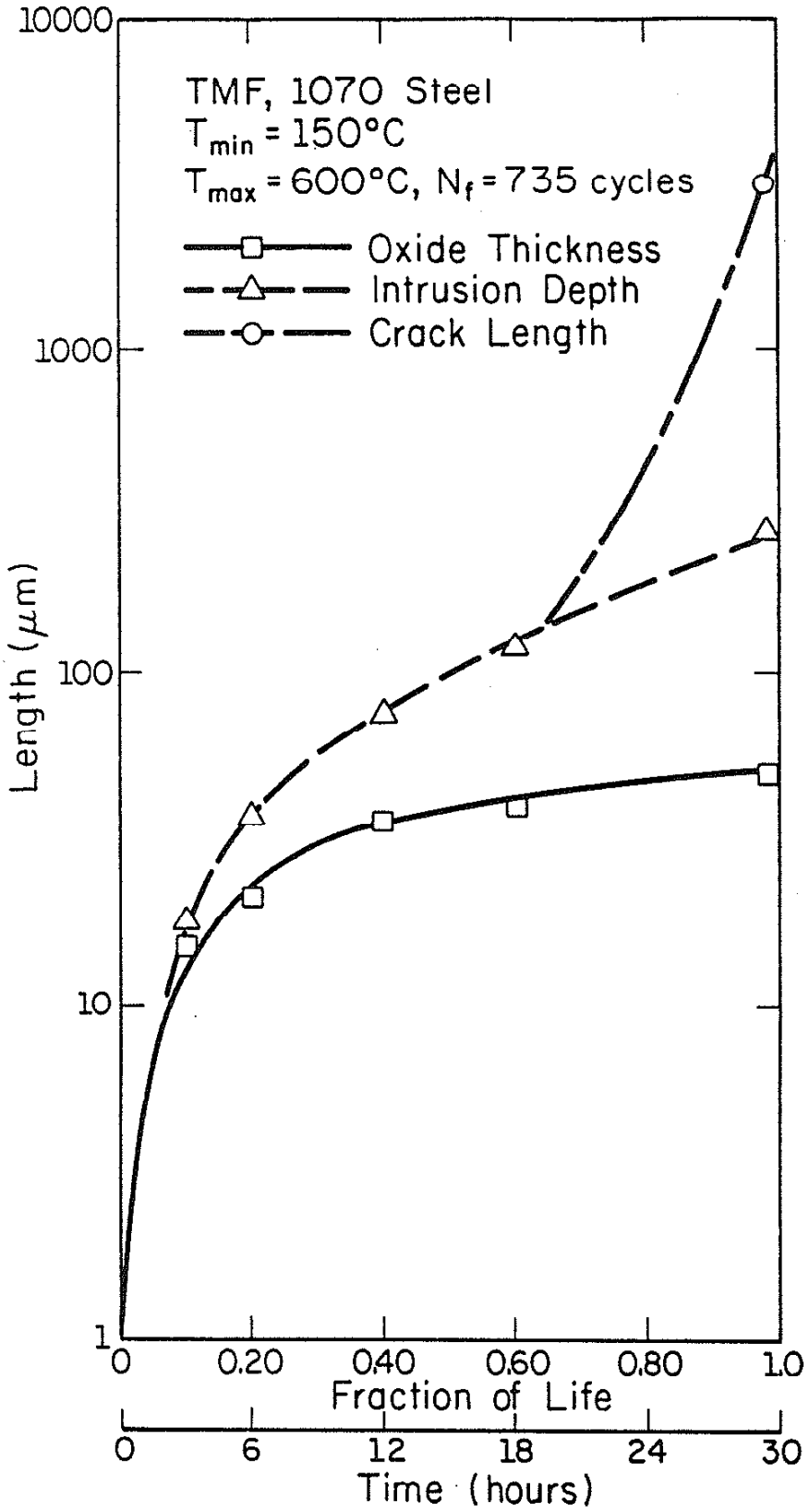

Figure 24 Oxide Thickness (h_o), Oxide Intrusion Depth (h_i), and Crack Length (a) during Thermo-Mechanical Fatigue Tests, T_{min} = 150°C, T_{max} = 600°C, $\dot{\varepsilon}_{av}$ = 0.0002 sec^{-1}

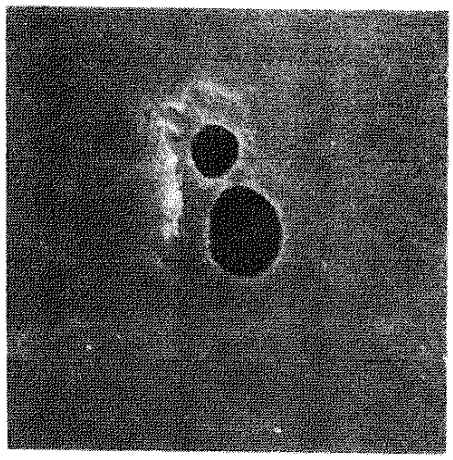

(a) Virgin sample
Test time = 0 hours

10 μm

(b) 10 percent of life
Test time = 3 hours

(c) 20 percent of life
Test time = 6 hours

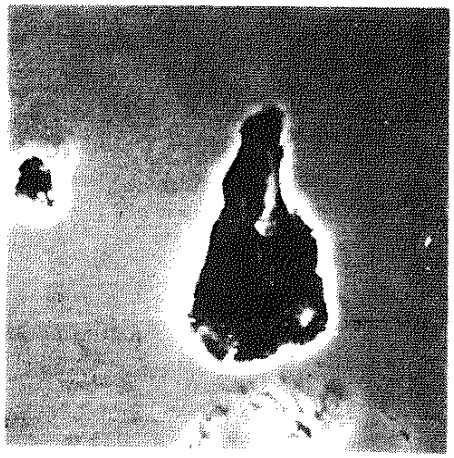

(d) 40 percent of life
Test time = 30 hours

Figure 25 Cavity Formation and Growth During Thermo-Mechanical Fatigue Tests, T_{min} = 150°C, T_{max} = 600°C, $\dot{\varepsilon}_{av}$ = 0.0002 sec^{-1}

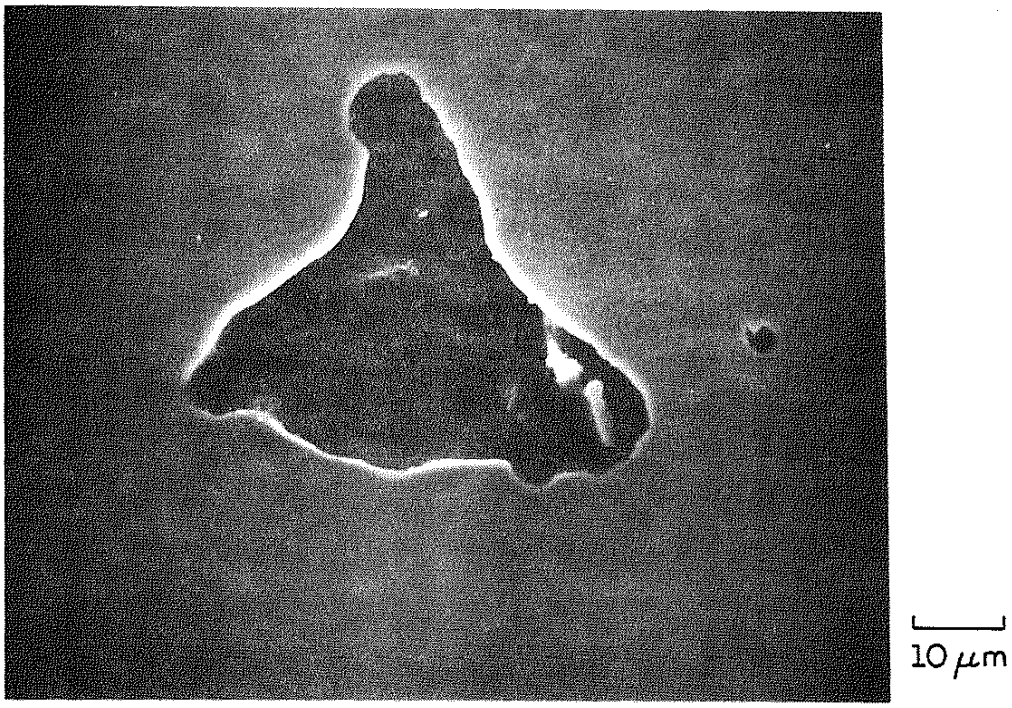

(e) 60 percent of life, Test time = 18 hours

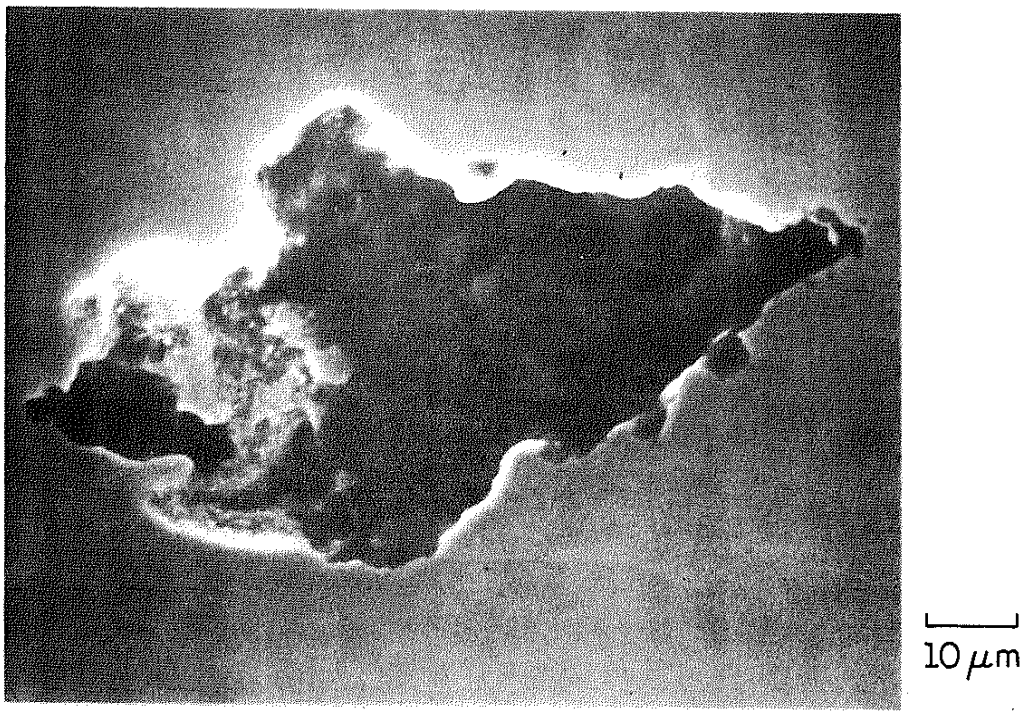

(f) 100 percent of life, Test time = 30 hours

Figure 25 (continued)

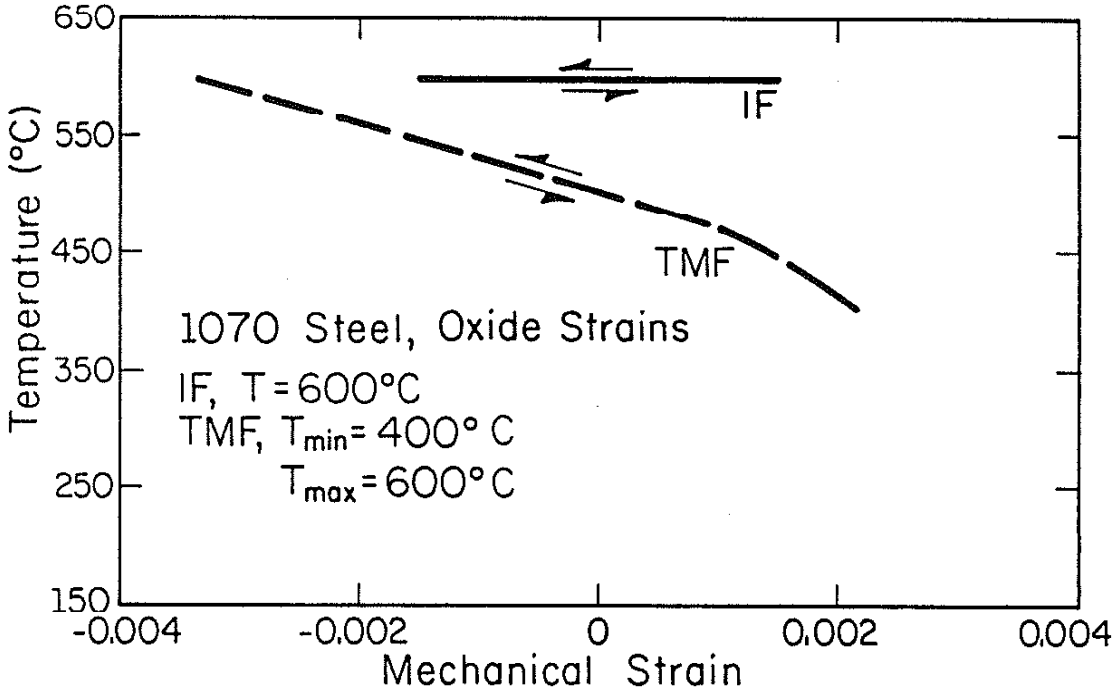

Figure 26 Axial Oxide Strains for IF and TMF (T_{mean} > 400°C)

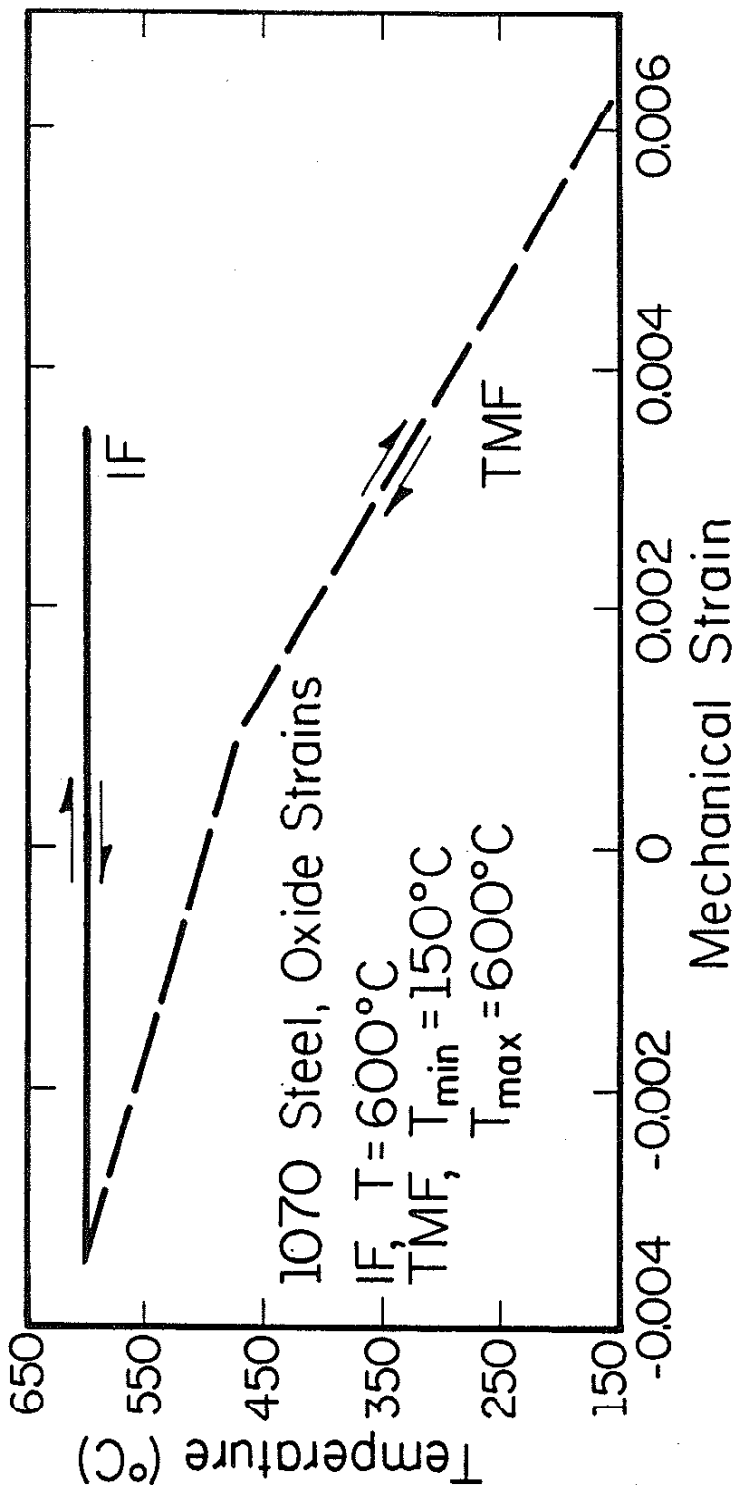

Figure 27 Axial Oxide Strains for IF and TMF (T_{mean} < 400°C)

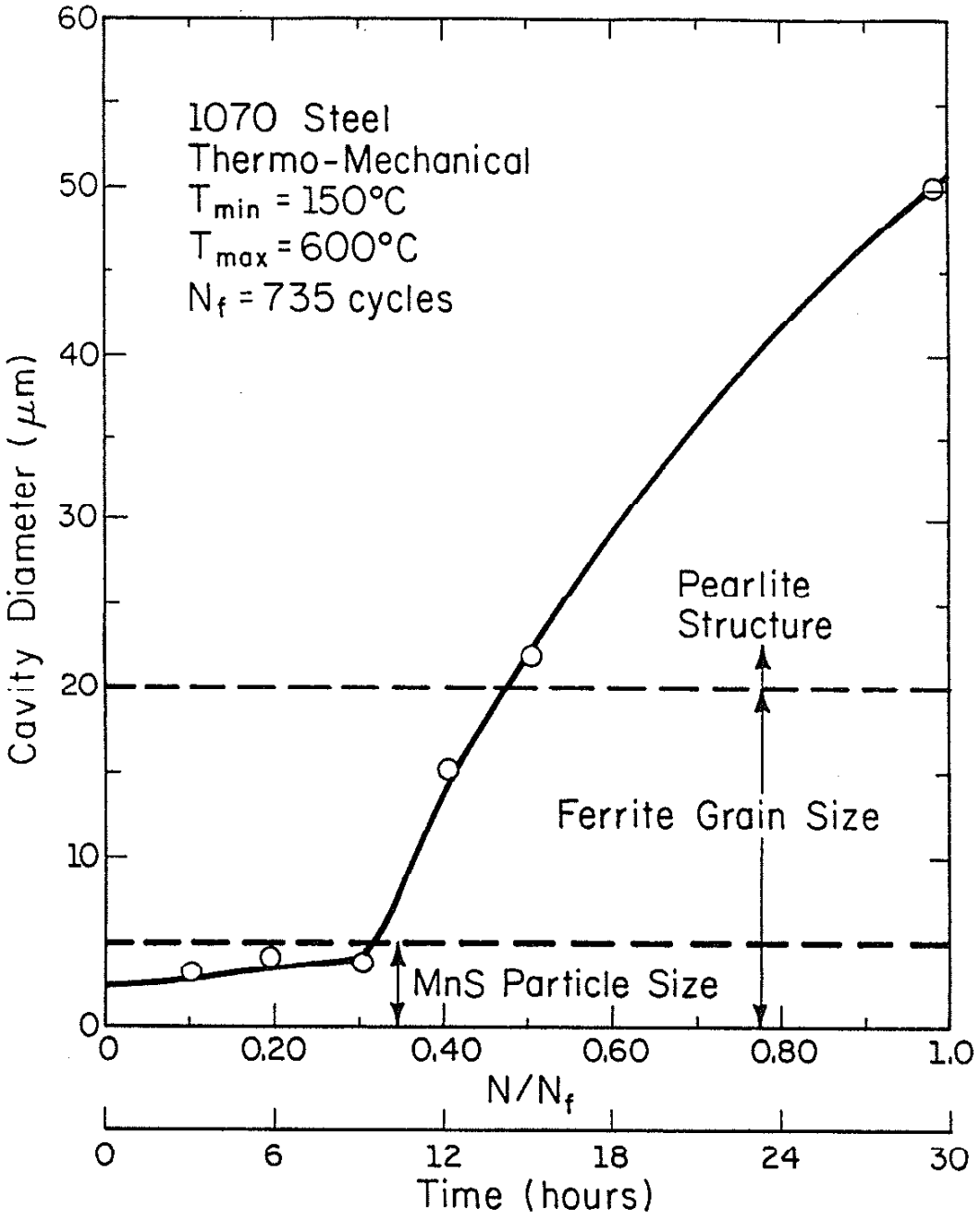

Figure 28 Cavity Growth during Thermo-Mechanical Fatigue Tests, T_{min} = 150°C, T_{max} = 600°C, $\dot{\varepsilon}_{av}$ = 0.0002 sec^{-1}

APPENDIX 1

Partial Pressure Calculations

The reactions under consideration include:

(a) $Fe_3C(s) + 2H_2(g) \rightarrow 3Fe(s) + CH_4(g)$

(b) $C(s) + O_2(t) \rightarrow CO_2(g)$

(c) $C(s) + \frac{1}{2} O_2(g) \rightarrow CO(g)$

(d) $MnS(s) + \frac{1}{2} O_2(g) \rightarrow MnO(s) + \frac{1}{2} S_2(g)$

(e) $MnS(s) + \frac{3}{2} O_2(g) \rightarrow MnO(s) + SO_2(g)$

The partial pressure, P, of the product gas in the above reactions is related to the fugacity of the reactions, f, and the activity coefficient, Γ, in the following manner [40]:

$$f = \Gamma P,$$

where the value of Γ is 1 for low partial gas pressures. For the general reaction,

$$A(s) + mB(g) \rightarrow C(s) + nD(g),$$

the partial pressure, P, of the product gas D may be calculated as follows [40]:

$$P_D^n = \frac{a_A}{a_C} K P_B^m ,$$

where $K = \exp(-\Delta G_o/RT)$. The values of the activities a_A and a_A are assumed to be approximately 1 in these calculations. For reactions (b) through (e), the values of G_o may be found in Ref. 53. For reaction (a), the value of K may be found directly in Ref. 54. Table A1 lists the values of G_o, K, P_B, and P_D for the reactions under consideration. The temperature used in all calculations was 600°C and the partial pressures of the reactant gases were assumed to be those found in the atmosphere.

Table A1

Reaction	ΔG_o	K (MPa^{-1})	P_B (MPa)	P_D (MPa)
(a)	-	2.9×10^{22}	5.0×10^{-8}	7.4×10^{7}
(b)	-94375	$3. \times 10^{23}$	0.02	6.0×10^{21}
(c)	-44989	1.5×10^{11}	0.02	6.7×10^{9}
(d)	-26100	3.1×10^{6}	0.02	1.9×10^{11}
(e)	-97600	1.9×10^{24}	0.02	1.7×10^{22}

REFERENCES

1. Kuwabara, W. and Nitta, A., "Effect of Strain Hold-Time of High Temperature on Thermal Fatigue Behavior of Type 304 Stainless Steel," 1976 ASME - MPC Symposium on Creep-Fatigue Interaction, R. M. Curran, ed., Dec. 1976.

2. Kawamoto, M., Tanaka, T. and Nakajima, H., "Effect of Several Factors on Thermal Fatigue," Journal of Materials, Vol. 1, No. 4, 1966, p. 719.

3. Lundberg, L. and Sandstrom, R., "Application of Low Cycle Fatigue Data to Thermal Fatigue Cracking," Scandinavian Journal of Metallurgy, Vol. 11, No. 2, 1982.

4. Jaske, C., "Thermal-Mechanical, Low-Cycle Fatigue of AISI 1010 Steel," Thermal Fatigue of Materials and Components, ASTM STP 612, D. Spera and D. Mowbray Eds., 1976, p. 170.

5. Udoguchi, T. and Wada, T., "Thermal Effect on Low-Cycle Fatigue Strength of Steels," Thermal Stresses and Thermal Fatigue, D. J. Littler, Ed., Butterworths, London 1971, p. 109.

6. Kuwabara, K. and Nitta, A., "Thermal-Mechanical Low-Cycle Fatigue Under Creep-Fatigue Interactions on Type 304 Stainless Steels," Fatigue of Engineering Materials and Structures, Vol. 2, 1979, p. 293.

7. Leis, B., Hopper, A., Ghadiali, N., Jaske, C. and Hulbert, G., "An Approach to Life Prediction of Domestic Gas Furnace Clam Shell Type Heat Exchangers," Thermal Stresses in Severe Environments, Hasselman and Heller, Eds., Plenum Pres, 1980, p. 207.

8. Taira, S., Fujino, M. and Ohtani, R., "Collaborative Study on Thermal Fatigue Properties of High Temperature Alloys in Japan," Fatigue of Engineering Materials and Structure, Vol. 1, 1979, p. 495.

9. Embley, G. T., and Russell, E. S., "Thermo-mechanical Fatigue of Gas Turbine Bucket Alloys," First Parsons International Turbine Conference, Dublin, Ireland, June 1984.

10. Baron, H., "Thermal Shock and Thermal Fatigue," Thermal Stress, Benham and Hoyle, Eds., Pitman Publishing Company, New York, 1964, p. 182.

11. Halford, G. R. and Manson, S. S., "Life Predictions of Thermal-Mechanical Fatigue Using Strain Range Partitioning," Thermal Fatigue of Materials and Components, ASTM STP 612, D. Spera and D. Mowbray Eds., 1976, p. 239.

12. Taira, S., "Relationship Between Thermal Fatigue and Low Cycle Fatigue at Elevated Temperature," ASTM STP 520, 1973, p. 80.

13. Sehitoglu, H., and Karasek, M., "Observations of Material Behavior Under Isothermal and Thermo-Mechanical Loading," Journal of Engineering Materials and Technology, Vol. 108, April 1986, pp. 192-198.

14. McGaw, M. A., "TMF Behavior of B1900 as Observed in Bithermal Experiments," TMF Workshop, NASA Lewis Research Center, Nov. 1984.

15. Karasek, M. L., "Material Behavior and Temperature History Interaction of Railroad Wheel Steel," T & A.M. Report No. 468, University of Illinois at Urbana-Champaign, July 1984.

16. Sehitoglu, H., "Material Behavior Under Thermal Loading," Journal of Pressure Vessel Technology, Vol. 108, February 1986, pp. 113-119.

17. Cook, R. H., and Skelton, R. P., "Environment-Dependence of the Mechanical Properties of Metals at High Temperatures," International Metallurgical Reviews, Vol. 19, Dec. 1974, pp. 199-222.

18. Skelton, R. P., "Crack Initiation and Growth in Simple Metal Components During Thermal Cycling," Fatigue at High Temperatures, ed. by R. P. Skelton, Appl. Sci. Pub., 1983, pp. 1-62.

19. Marshall, P., "The Influence of Environment on Fatigue," Fatigue at High Temperatures, ed. by R. P. Skelton, Appl. Sci. Pub., 1983, pp. 259-303.

20. Hancock, P., and Hurst, R. C., "The Mechanical Properties and Breakdown of Surface Oxide Films at Elevated Temperatures," Adv. in Corrosion Science and Technology, Vol. 4, Plenum Press, 1974.

21. Stringer, J., "Stress Generation and Relief in Growing Oxide Films," Corrosion Science, Vol. 10, 1970, pp. 513-543.

22. Birks, N., and Meier, G. H., Introduction to High Temperature Oxidation of Metals, Edward Arnold Publishers, London, 1983.

23. Douglas, D. L., "Exfoliation and the Mechanical Behavior of Scales," Oxidation of Metals and Alloys, American Society for Metals, Metals Park, Ohio, October 1970, pp. 137-156.

24. Evans, H. E., "The Role of Oxide Grain Boundaries in the Development of Growth Stresses During Oxidation," Corrosion Science, Vol. 23, No. 5, 1983, pp. 495-506.

25. Caplan, D. and Cohen, M., "Effect of Cold Work On the Oxidation of Iron From 400-650°C," Corrosion Science. Vol. 6, 1966, p. 321.

26. Mackenzie, J. and Birchenall, C., "Plastic Flow of Iron Oxides and the Oxidation of Iron," Corrosion, Vol. 13, No. 12, 1957, p. 783.

27. Price, W. R., "On the Effect of Cold Work on the Oxidation of Iron From 400° to 650°C," Corrosion Science, Vol. 7, 1967, p. 473.

28. Manning, M. E., "Geometrical Effects on Oxide Scale Integrity," Corrosion Science, Vol. 21, No. 4, 1981, p. 301.

29. Bruce, D. and Hancock, P., "Influence of Specimen Geometry on the Growth and Mechanical Stability of Surface Oxides Formed on Iron and Steel in the Temperature Range 570°-800°C," Journal of Iron and Steel Institute, November 1970, p. 1021.

30. Bruce, D. and Hancock, P., "Mechanical Properties and Adhesion of Surface Oxide Films on Iron and Nickel Measured During Growth," Journal of the Institute of Metals, Vol. 94, 1969, p. 148.

31. Caplan, D., Sproule, G., Hussey, R., and Graham, M., "Oxidation of Fe-C Alloys at 500°C," Oxidation of Metals, Vol. 12, No. 1, 1978, p. 67.

32. Caplan, D., Sproule, G., Hussey, R., and Graham, M., "Oxidation of Fe-C Alloys at 700°C," Oxidation of Metals, Vol. 13, No. 3, 1979, p. 255.

33. Malik, A. and Whittle, D., "Oxidation of Fe-C Alloys in the Temperature Range 600-850°C," Oxidation of Metals, Vol. 16, Nos. 5/6, 1981, p. 339.

34. Skelton, R., "Environmental Crack Growth in 0.5Cr-Mo-V Steel During Isothermal High Strain Fatigue and Temperature Cycling," Materials Science and Engineering, Vol. 35, No. 2, 1978, p. 287.

35. Forrest, J. E., and Bell, P. S., "The Relationship Between the Deformation of Substrate and Scale in the Mechanism of Multilayer Oxide Formation on Low Alloy Ferritic Steels," European Symposium on the Interaction Between Corrosion and Mechanical Stress at High Temperatures," Patten, The Netherlands, May 1980.

36. Bell, P. S., and Forrest, J. E., "Laminated Scale Growth on 2¼ CrMo Steel and Its Role in Oxide Jacking," Central Electricity Generating Board, RD/L/R 2009, February 1980.

37. Challenger, K. D., Miller, A. K., and Brinkman, C. R., "An Explanation for the Effects of Hold Periods on the Elevated Temperature Fatigue Behavior of 2¼ Cr-1 Mo Steel," ASME Journal of Engineering Materials and Technology, Vol. 103, January 1981, pp. 7-14.

38. Manson, S. S., Halford, G. R., and Oldrieve, R. E., "Relation of Cyclic Loading Pattern to Microstructural Fracture in Creep Fatigue," NASA Technical Memorandum 83473, 1984.

39. Skelton, R. and Bucklow, J., "Cyclic Oxidation and Crack Growth During High Strain Fatigue of Low Alloy Steel," Metal Science, February 1978, p. 64.

40. Raj, R., "Intergranular Creep Fracture in Aggressive Environments," Acta Metallurgica, Vol. 30, 1982, pp. 1259-1268.

41. Parthasarathy, T. A., "Mechanisms of Hydrogen Attack of Carbon and 2½Cr-1Mo Steels," Acta Metallurgica, Vol. 33, No. 9, 1985, pp. 1673-1681.

42. Wetenkamp, H. R., Sidebottom, O. M., and Schraeder, H. J., "The Effect of Brake Shoe Action on Thermal Checking and on Failure of Wrought Steel Railway Car Wheels," University of Illinois Engineering Experiment Station Bulletin No. 387, Urbana, June 1950.

43. Bauling, F. G., "The Effect of Elevated Temperatures on Mechanical Properties of Wrought Steel Railway Car Wheel Material," Master of Science Thesis, University of Illinois, Urbana, 1953.

44. Wetenkamp, H. R., and Kipp, R. M., "Thermal Damage and Rail Load Stresses in a 33-inch Railroad Car Wheel," ASME Paper No. 77-WA/RT-2.

45. Kipp, R. M., "Investigations of Crack Growth in Railroad Car Wheels Caused by Thermally Induced Residual Stress Changes and Cyclic Mechanical Loading," T&A.M. Report No. 428, University of Illinois at Urbana-Champaign, August 1978.

46. Fec, M. C., "Thermal Fatigue of Class "U" Cast Wheel Steels," Master of Science Thesis, Illinois Institute of Technology, Chicago, Illinois, December 1980.

47. Sehitoglu, H., "Constraint Effect in Thermo-mechanical Fatigue," ASME Journal of Engineering Materials and Technology, Vol. 107, 1985, pp. 221-226.

48. Morrow, JoDean," Cyclic Plastic Strain Energy and Fatigue of Metals," Society for Testing and Materials, Philadelphia, 1965, pp. 45-87.

49. Karasek, M., Sehitoglu, H., and Slavik, D., "Deformation and Damage Under Thermal Loading," ASTM Conference on Low Cycle Fatigue, Lake George, New York, October 1985.

50. Slavik, D., Forthcoming Master of Science Thesis, University of Illinois at Urbana-Champaign, 1986.

51. Frank, W., Engell, H. J., and Seeger, A., "Solubility and Interstitial Migration of Oxygen in BCC Iron," Trans. of Metal. Society of AIME, Vol. 242, April 1968, pp. 749-750.

52. Frost, H. J., and Ashby, M. F., Deformation-Mechanism Maps, Pergamon Press, New York, 1982.

53. Kubaschewski, Evans, Alco, Metallurgical Thermochemistry, 4th Edition, Vol. 1, International Series of Monographs in Metal Physics and Physical Metallurgy, Ed. G. V. Raynor, Pergamon Press, 1967.

54. Geiger, F. H., and Angelis, O. F., API Publication No. 945, 1975.